

# Linear models for sound from supersonic reacting mixing layers

P. Shivakanth Chary and Arnab Samanta\*

*Department of Aerospace Engineering, Indian Institute of Science, Bangalore 560012, India*

(Received 11 April 2016; published 21 December 2016; corrected 6 February 2017)

We perform a linearized reduced-order modeling of the aeroacoustic sound sources in supersonic reacting mixing layers to explore their sensitivities to some of the flow parameters in radiating sound. Specifically, we investigate the role of outer modes as the effective flow compressibility is raised, when some of these are expected to dominate over the traditional Kelvin-Helmholtz (K-H) -type central mode. Although the outer modes are known to be of lesser importance in the near-field mixing, how these radiate to the far-field is uncertain, on which we focus. On keeping the flow compressibility fixed, the outer modes are realized via biasing the respective mean densities of the fast (oxidizer) or slow (fuel) side. Here the mean flows are laminar solutions of two-dimensional compressible boundary layers with an imposed composite (turbulent) spreading rate, which we show to significantly alter the growth of instability waves by saturating them earlier, similar to in nonlinear calculations, achieved here via solving the linear parabolized stability equations. As the flow parameters are varied, instability of the slow modes is shown to be more sensitive to heat release, potentially exceeding equivalent central modes, as these modes yield relatively compact sound sources with lesser spreading of the mixing layer, when compared to the corresponding fast modes. In contrast, the radiated sound seems to be relatively unaffected when the mixture equivalence ratio is varied, except for a lean mixture which is shown to yield a pronounced effect on the slow mode radiation by reducing its modal growth.

DOI: [10.1103/PhysRevFluids.1.083801](https://doi.org/10.1103/PhysRevFluids.1.083801)

## I. INTRODUCTION

Combustion noise, as a component of overall sound from turbofan engines [1], typically assumes prominence over the fan and jet noise sources at broad levels of moderate frequencies (e.g.,  $\sim 300$ – $1000$  Hz during an aircraft approach) [2,3]. The recent shift to newer combustion technologies, e.g., lean premixed prevaporized combustion in commercial gas turbines, has further increased its importance due to such processes being inherently more unsteady, resulting in a greater probability of increased combustion noise [4]. Such combustor designs are also susceptible to self-sustained oscillations, possibly leading to combustion instability, where these same acoustic waves are crucial in establishing a feedback loop with the unsteady combustion heat release [5]. Better understanding of the sources and propagation of acoustic waves directly or indirectly linked to the combustion process is therefore important in more efficient modern combustor designs.

In this work, we model combustion in nonpremixed open flames via a set of two-dimensional reacting mixing layers with infinitely fast, single-step chemistry. Practical combustors may encounter thermoacoustic instabilities [5], but the basic mechanism of aerodynamic sound generation remains unaltered, which still hinges on an accurate description of flow dynamics dominated by large-scale coherent structures, known to be the main contributor to peak radiated sound even for reacting flows [6–8]. In general, for nonpremixed flames this sound field seems to be less well understood, perhaps because of the difficulty in setting up reliable experimental measurements [9], whereas the associated complexity involved in numerical modeling has also restricted it to fewer studies [6–8,10,11].

Supersonic combustion presents additional challenges, where none of the traditional low-Mach number simplifications used in combustion modeling hold, including that for the chemical source

---

\*samanta@aero.iisc.ernet.in

terms. However, with our primary interest being quantifying the radiated sound, we instead focus on advanced modeling of the hydrodynamic sound sources, which has not been attempted in any great detail for supersonic diffusion flames. Previously, sound sources in turbulent flames have been modeled as uncorrelated monopoles [12], generalized later as inputs to a Lighthill’s acoustic analogy-type formulation [7,8,11,13,14], with the mean flow fields usually obtained from direct [14] or large eddy simulations [7,8,11]. In this work, without using any acoustic analogy, we follow a *direct* approach where sound sources are modeled using physics-based reduced-order models, *viz.*, the parabolized stability equation (PSE) [15,16], which additionally provides reliable predictions for the radiated sound at supersonic wave speeds, as discussed below.

The primary radiated sound from nonreacting mixing layers have long been associated with the linear and nonlinear instabilities of the large-scale coherent structures [17–23], depending in turn on the factors that affect their growth, which include but are not limited to the flow compressibility [24–29]. The mixing layer spread rate is defined to be a function of the convective Mach number  $M_c$  [see (1) for a definition], which loosely translates to the convection speed of large turbulent structures in the flow. However, nonisothermal mixing layers, especially the reacting ones, are more complicated by the fact that they include additional parameters that may have influence on their growth rates, including density ratio, mixture equivalence ratio, and chemical heat release, with all of these potentially having bearing on the nature of their acoustic spectra, as has been shown before for premixed flames [30]. In this work, we aim to systematically investigate the role of these additional parameters on the radiated sound from supersonic reacting mixing layers, intended as a model for supersonic diffusion flames.

The large-scale coherent structures observed in the shear layers of canonical flows may be mathematically modeled via wave packets whose evolution is conveniently tracked using a linear stability analysis [31–36]. Although fast and convenient, the accuracy of traditional linear stability theory in predicting the near-field wave packets may be significantly improved by opting for a system of equations that offer slow streamwise divergence of flow, e.g., the PSE [15,16,23,37–42]. However, in the context of sound generation, the PSE-modeled wave packets are known to severely underpredict the far-field sound, which has led to hypotheses where nonlinearity and intermittency are believed to be important factors [43,44], providing impetus to the development of nonlinear PSE-based models [19,21–23]. Interestingly, coherent structures convected at supersonic speeds, like we investigate here, are less likely to be affected by the nonlinearities of the model [23,42,45], which has motivated us to continue with a linearized PSE approach. Later, we demonstrate the effectiveness of our linear model in simulating supersonic mixing layers by comparing it with calculations that include nonlinearity (see Appendix A). In using a PSE-based reduced-order model of compressible, reacting mixing layers with fast chemistry, our work follows Day *et al.* [38] except it differs in the important aspect of using a composite spread rate for the mean mixing layer, as we discuss next. Note that sound radiation from subsonic and supersonic cold mixing layers have been studied in detail by Cheung and Lele [23], who used nonlinear PSE to model the near field sources.

The nature of mixing layer spreading plays an important role in the evolution of large scale structures. For example, normal mode studies of shear flows that include a laminar (or transitional) spread rate [23,38,46] require a mean-flow correction to correctly capture the growth and eventual saturation of the most energetic modes, which otherwise are grossly overestimated by a linear theory [23]. In essence, this procedure introduces the nonlinear modal interactions into a laminar base flow, which for a turbulent base flow is presumed to be already present. Indeed, for practical flows with turbulent means it is the linear instability waves which are expected to play the dominant role in their instability [47], perhaps making the nonlinear processes in fluctuations less relevant [41]. In this work, laminar, compressible boundary layer equations are used for the base flow, where nonlinear interactions are indirectly introduced via the following procedure. In this process, a composite spreading curve for the initially laminar mean mixing layer is employed that smoothly varies from a laminar to turbulent spreading as described in Sec. II B, using data available from the evolution of similar compressible mixing layers. This directly inducts a transitional zone, which we show to be critical in correct estimation of Mach radiation from supersonic mixing layers. Such a spread rate

saturates the growing linear instabilities, in a manner similar to nonlinear evolution of mixing layers, without actually solving for any of the nonlinear terms.

The instabilities of incompressible shear flows usually refer to the K-H instability, which at increased levels of compressibility (i.e., higher  $M_c$ ), as is the interest here, may be augmented by two additional modes, corresponding to each of the two streams [38,48,49]. The appearance of these new modes, referred to as the “outer” modes (when compared to the “central” K-H mode), is attributed to the extra peaks in the corresponding density-weighted vorticity profiles for high  $M_c$  mixing layers [38,49], whose dominance is expected to be further enhanced for reacting layers with sufficiently high heat release [50–52]. Once the phase speeds of any of these outer modes are supersonic with respect to the local speed of sound they are expected to radiate efficiently as Mach waves [53,54]. Although the effect of increased compressibility on the growth rate of the K-H mode (and hence the radiated sound) is known to be stabilizing [55], increased heat release sometimes has a less than pronounced effect [56]. Moreover, as will be shown, the criticality of outer modes depends largely on the location of flame surface and the associated shear, phenomena that are dynamically different from the central mode, so that their evolution as heating and other parameters are varied is not easy to anticipate. For example, incompressible reacting mixing layers at higher levels of heat release show a jump in growth rates after being initially attenuated [57], perhaps due to increased dominance of outer modes. On the other hand, a recent study on subsonic mixing layers found increased heating of the fast side to actually reduce the far-field sound at the slower side, attributed to cancellations in the source terms [58]. In this work, we restrict ourselves to cases when *at least* one of the outer modes is supersonic relative to the corresponding stream but investigate in detail their role in Mach radiation as the basic properties of reacting mixing layers are varied.

The model problem and governing and reduced equations are briefly described in Sec. II A, and the laminar mean flow equations and the composite spread models are discussed in Sec. II B. A short description on the Lilley-Goldstein sound sources is in Sec. II C, used to quantify the aeroacoustic sources as obtained from the PSE solutions. The boundary and initial conditions and some numerical details are highlighted in Secs. II D and II E, respectively. The classification scheme used in this work for the unstable modes is in Sec. III A, which also provides motivation for all the cases studied. The fast and slow mode results are described in detail in Sec. III B, and the colayer cases, introduced in Sec. III A, are briefly touched upon in Sec. III C. Section IV summarizes our work, Appendices A and B detail validation results and mean flow computations, respectively, Appendix C describes a brief sensitivity study on the proposed composite spread model, and the detailed PSE operators are in Appendix D.

## II. FORMULATION AND METHODOLOGY

### A. Compressible stability equations

The model flow configuration of a two-dimensional reacting mixing layer is shown in Fig. 1. The upper high-speed stream (henceforth denoted by subscript 1) has an oxidizer mass fraction of  $Y_{O,\infty}$  with density  $\rho_1^*$  and velocity  $U_1^*$ . The lower slow-speed stream (denoted by subscript 2) carries fuel at a mass fraction of  $Y_{F,-\infty}$ , density  $\rho_2^*$ , and velocity  $U_2^*$ , where (\*) denote dimensional quantities. The subscripts  $F$  and  $O$  identify the fuel and oxidizer, respectively. The density ratios and velocity ratios between the two streams are denoted by the parameters  $\kappa_\rho = \rho_2^*/\rho_1^*$  and  $\kappa_U = U_2^*/U_1^*$ , respectively. The convection speed and the convective Mach number of the mixing layer are defined as [23,55]

$$U_c = \frac{a_2^* U_1^* + a_1^* U_2^*}{a_1^* + a_2^*}, \quad M_c = \frac{U_1^* - U_2^*}{a_1^* + a_2^*}, \quad (1)$$

where  $a_1^*$  and  $a_2^*$  are the speed of sound in the upper and lower streams, respectively.

The flow is governed by the viscous, compressible-fluid equations and the equation of state in two dimensions ( $x, y$ ) under the assumption of infinitely fast chemistry that drops out the chemical production terms from the species mass fraction ( $Y_F, Y_O$ ) equations, while the mass

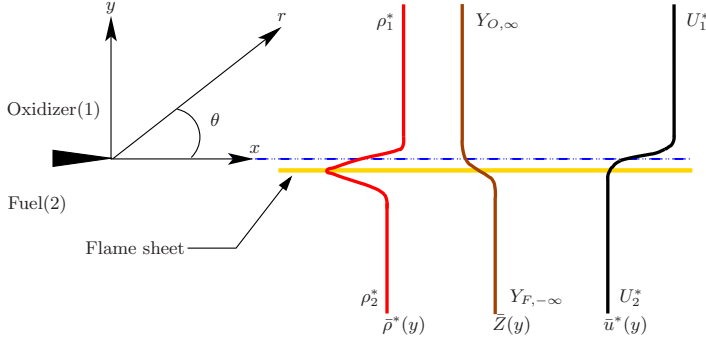


FIG. 1. Schematic of two-dimensional reacting mixing layer configuration showing typical mean profiles for density  $\bar{\rho}^*$ , conserved scalar  $\bar{Z}$ , and streamwise velocity  $\bar{u}^*$ , with their corresponding free stream values labeled (see text). The flame sheet is indicated by a thick horizontal line (here representative of a lean mixture). The far-field sound is expressed in  $(r, \theta)$  coordinates fixed at the splitter edge.

fractions themselves may be coupled via a conserved passive scalar [38]

$$Z = Y_F - Y_O/n, \quad (2)$$

where  $n$  is the ratio of stoichiometric coefficients between oxidizer and fuel as per the single-step, single-product overall chemical reaction considered here [59]:



where, additionally, the subscript  $P$  identifies the product. Note that the form of conserved scalar in Eq. (2) is different from the classical definition of mixture fraction [59], although it may be readily derived from the latter. The present scalar variable varies from a positive constant at the fuel stream to a negative constant in the oxidizer (see Fig. 1), their respective values depend upon the chosen parameters, with  $Z = 0$  at stoichiometric concentrations. In our calculations, a uniform molecular mass assumption is used [also in Eq. (2)], simplifying the analysis greatly, practically achieved by appropriately diluting the fuel and oxidizer streams with, say, nitrogen. The use of fast chemistry over any detailed chemistry calculations is preferred, since apart from the known difficulty in implementing the latter in time-periodic Fourier-space stability calculations, these extra equations seem to have any role on the development of instabilities only at higher perturbation frequencies [60], not so much at the lower frequencies considered in this work (see in Sec. III) that are relevant to the large-scale coherent structures and their radiated sound. Now, assuming constant specific heats and nondimensionalizing with respect to the fast-side quantities with the initial mean vorticity thickness  $\delta_w^*|_0$  as the length scale, where

$$\delta_w^* = \frac{(U_1^* - U_2^*)}{|d\bar{u}^*/dy^*|_{\max}}, \quad (4)$$

with  $\bar{u}$  being the mean streamwise velocity, yields

$$\frac{\partial \rho}{\partial t} + \frac{\partial \rho u_i}{\partial x_i} = 0, \quad (5a)$$

$$\rho \left( \frac{\partial u_i}{\partial t} + u_j \frac{\partial u_i}{\partial x_j} \right) = -\frac{1}{\gamma M_1^2} \frac{\partial p}{\partial x_i} + \frac{1}{\text{Re}} \frac{\partial \tau_{ij}}{\partial x_j}, \quad (5b)$$

$$\rho \left( \frac{\partial T}{\partial t} + u_i \frac{\partial T}{\partial x_i} \right) = -p(\gamma - 1) \frac{\partial u_i}{\partial x_i} + \frac{\gamma}{\text{PrRe}} \frac{\partial}{\partial x_i} \left( \mu \frac{\partial T}{\partial x_i} \right) + \gamma(\gamma - 1) \frac{M_1^2}{\text{Re}} \Phi, \quad (5c)$$

$$\rho \left( \frac{\partial Z}{\partial t} + u_i \frac{\partial Z}{\partial x_i} \right) = \frac{1}{\text{LePrRe}} \frac{\partial}{\partial x_i} \left( \mu \frac{\partial Z}{\partial x_i} \right), \quad (5d)$$

$$p = \rho T, \quad (5e)$$

where  $u_i \equiv (u, v)$ ,  $x_i \equiv (x, y)$  with the following nondimensional numbers appearing: Mach number  $M_k = U_k^*/a_1^*$ , corresponding to each of the streams  $k \equiv 1, 2$ , Reynolds number  $\text{Re} = U_1^* \delta_w^* |0|/\nu^*$ , Prandtl number  $\text{Pr} = \nu^*/\alpha^*$ , and Lewis number  $\text{Le} = \lambda^*/\mathfrak{D}^*$ , the last two assumed unity in this work. Further,  $\nu = \mu^*/\rho^*$  is the kinematic viscosity,  $\lambda^*$  is the thermal diffusivity,  $\mathfrak{D}^*$  is the molecular diffusivity, and  $\gamma = 1.4$  is the ratio of specific heats, whereas the viscous tensor  $\tau_{ij}$  and viscous dissipation  $\Phi$  satisfy

$$\tau_{ij} = \mu \left( \frac{\partial u_i}{\partial x_j} + \frac{\partial u_j}{\partial x_i} - \frac{2}{3} \frac{\partial u_k}{\partial x_k} \delta_{ij} \right), \quad (6a)$$

$$\Phi = \tau_{ij} \frac{\partial u_i}{\partial x_j}, \quad (6b)$$

with  $\mu = T$ , amounting to a Chapman approximation. Of course, there are other more detailed models of thermo-viscous properties available, but at the low perturbation frequencies of this work such choices are not expected to matter [60].

Linear stability equations are obtained by splitting the flow variables  $\mathbf{q} = [\rho \ u \ v \ T \ Z]^T$  into a mean  $\bar{\mathbf{q}}$  and fluctuation  $\mathbf{q}'$ , with the product of fluctuations neglected. The mean pressure is assumed to be unity throughout, which directly relates  $\bar{\rho}$  to  $\bar{T}$  via (5e). In the PSE, the fluctuations are modeled via [15,16,61]

$$\mathbf{q}'(x, y, t) = \sum_n \hat{\mathbf{q}}_n(x, y) \exp(-i\omega_n t) = \sum_n \tilde{\mathbf{q}}_n(x, y) \exp[i(\int^x \alpha_n(\xi) d\xi - \omega_n t)], \quad (7)$$

where  $\omega_n = n\omega_0$ , with  $\omega_0$  being the base frequency,  $\alpha_n = \Re(\alpha_n) + i\Im(\alpha_n)$  is the complex wave number and  $\tilde{\mathbf{q}}_n(x, y)$  is the shape function with a ‘‘slow’’ streamwise evolution. In a spatial stability analysis, the quantities  $\Re(\alpha_n)$  and  $\Im(\alpha_n)$  are, respectively, the streamwise wave number and growth rate, with the latter deciding on the stability. Here we mostly consider two-dimensional fluctuations of the form (7), except in one central-mode-dominated case where the most unstable mode is three-dimensional, which requires an  $\exp(i\beta_m z)$  factor to be introduced in Eq. (7), where  $\beta_m$  is now the spanwise wave number with  $\beta_m = m\beta_0$ .

Substituting (7) into (5) yields

$$[A(\bar{\mathbf{q}}, \omega_n, \alpha_n) + B(\bar{\mathbf{q}})]\tilde{\mathbf{q}} + C(\bar{\mathbf{q}}) \frac{\partial \tilde{\mathbf{q}}}{\partial x} + D(\bar{\mathbf{q}}) \frac{\partial \tilde{\mathbf{q}}}{\partial y} = \frac{1}{\text{Re}} E(\bar{\mathbf{q}})\tilde{\mathbf{q}}, \quad (8)$$

where it has been assumed that  $\partial^2 \tilde{\mathbf{q}}/\partial x^2 \equiv 0$  to account for the slow streamwise variation of the eigenfunctions. The viscous terms in  $E$  are further simplified using a thin-shear-layer approximation where only the cross-stream derivatives are retained. The details of the operator  $A$  to  $E$  appear in Appendix C, where it may be noted that because of the simplifications made above, the conserved scalar fluctuations have been decoupled from the fluctuations in density, velocities, and temperature. In other words, density fluctuations as obtained via solving (8) do not include any contribution from chemical reactions [62], so that the effect of combustion on stability modes is solely via the modulation of mean quantities, as discussed in the next section.

Whether a particular instability mode radiates to the far field as Mach waves depends on its ability to propagate at a supersonic phase speed, which may be characterized via a relative Mach number  $\bar{M}_{n,k}$  for the mode  $(\omega_n, \alpha_n)$  in the respective stream  $k$ , where

$$\bar{M}_{n,1} = M_1 |\omega_n/\Re(\alpha_n) - 1| \quad \text{and} \quad \bar{M}_{n,2} = M_1 \sqrt{\kappa_\rho} |\omega_n/\Re(\alpha_n) - \kappa_U|, \quad (9)$$

with  $\bar{M}_{n,k} > 1$  indicating the mode radiating in the corresponding stream as Mach waves.

## B. Mean flow

The mean flow  $\bar{\mathbf{q}}$  in Eq. (8) is obtained from the steady, two-dimensional, compressible boundary layer equations [63], which may be deduced from (5) by neglecting the streamwise pressure gradient.

When written in terms of a stream function  $\psi$  such that  $\rho\bar{u} = \partial\psi/\partial y$  and  $\rho\bar{v} = -\partial\psi/\partial x$  these equations yield [38]

$$\frac{\partial\psi}{\partial y} \frac{\partial\bar{q}}{\partial x} - \frac{\partial\psi}{\partial x} \frac{\partial\bar{q}}{\partial y} = \frac{1}{\text{Re}} \frac{\partial}{\partial y} \left( \mu \frac{\partial\bar{q}}{\partial y} \right), \quad (10)$$

where  $\bar{q} = [\bar{u} \ \bar{h}_t \ \bar{Z}]^T$ , with the mean energy written in terms of total enthalpy  $\bar{h}_t$  containing the chemical, thermal, and kinetic energies.

The thermal and chemical portions of  $\bar{h}_t$  may be simplified following standard procedures to yield the adiabatic flame temperature  $\bar{T}_c^*$  [59] such that

$$\bar{T}_c^* = \bar{T}_1^* - \frac{q_c^* \bar{Y}_{F,-\infty}}{c_{p_1}^* (1 + \phi)}, \quad (11)$$

where,  $q_c^*$  is the heat released per unit fuel mass,  $c_{p_1}^*$  is the constant specific heat, and  $\bar{T}_1^*$  the ‘‘frozen’’ mean temperature of the oxidizer side. The equivalence ratio  $\phi$ , a ratio of fuel-air ratios between real and stoichiometric mixtures, reduces here to

$$\phi = \frac{n \bar{Y}_{F,-\infty}}{\bar{Y}_{O,\infty}}. \quad (12)$$

A nondimensional heat release parameter may now be readily constructed from (11) via

$$\Theta = \frac{-q_c^* \bar{Y}_{F,-\infty}}{c_{p_1}^* \bar{T}_1^* (1 + \phi)}, \quad (13)$$

which is identical to the one used in Day *et al.* [38] Although as per (3),  $q_c^*$  is given by

$$-q_c^* = h_{f,F}^* + n h_{f,O}^* - (n + 1) h_{f,P}^*, \quad (14)$$

where  $h_{f,i}^*$  are heat of formations of species  $i$ , in this work, for a given  $\Theta$  and  $\phi$ , we simply assume a single chemical reference species to combine the effects of fuel, oxidizer, and product, simply denoted by  $h_{f,F}^*$ , which is then used to compute the mean temperature profile [see (B1)]. Also, note that in a linear analysis like we do here, specifics of (3) or the actual values of  $c_{p_1}^*$  and  $\bar{T}_1^*$  are unimportant and can be taken arbitrary.

The classical way of solving (10) is by introducing similarity parameters  $(\xi, \eta)$  [64] via

$$\xi = x^n \quad \text{and} \quad \eta = \frac{1}{f(\xi)} \int_0^y \rho \, dy, \quad (15)$$

where the exponent  $n$  maps the flow spreading along the streamwise  $x$  direction, allowing for different flow regimes to be included within the same framework, while the function  $f(\xi)$  also includes  $\text{Re}$  as a parameter. In this way, Eq. (15) may be regarded as a generalized version of the well-known Howarth’s transformation [64], which now directly accommodates nonlaminar mean spread rates in the analysis on setting  $n \neq 1$ . For laminar mean flow  $n = 1$ , and in addition

$$f(\xi) = \sqrt{\frac{2\xi}{\text{Re}}} \quad (16)$$

yields

$$F''' + FF'' = 0, \quad \bar{h}_t'' + F\bar{h}_t' = 0, \quad \bar{Z}'' + F\bar{Z}' = 0, \quad (17)$$

where  $\bar{Z}$  and  $\bar{h}_t$  are now functions of  $\eta$  only with  $F(\eta) = \psi(x,y)/f(\xi)$ . Here  $(\prime)$  indicates differentiation with respect to  $\eta$ . The system of equations (17) are identical to the mean equations of Day *et al.* [38], which are solved in a similar fashion described briefly in Appendix B. A composite spreading curve, as discussed next, is superimposed on these mean solutions to yield their streamwise evolution.

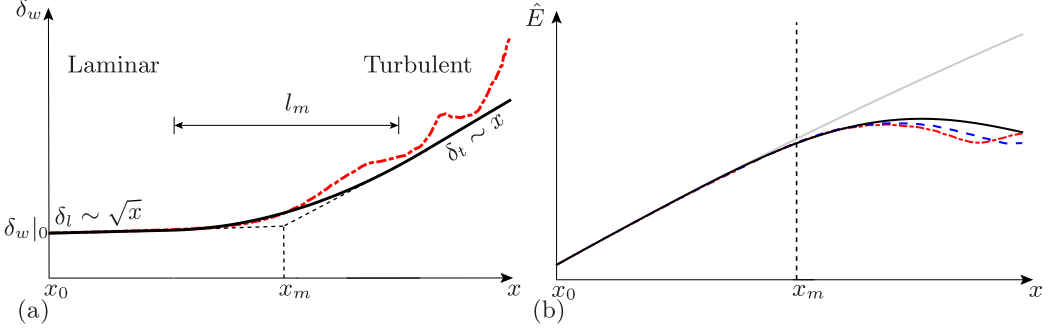


FIG. 2. Streamwise evolution of (a) the mean vorticity thickness and (b) the most unstable mode in a cold mixing layer  $M_c = 0.5, \kappa_\rho = 1, \kappa_U = 0.6$  [38,65], shown for the following mean flows: — linear PSE with composite spread, - · - · - nonlinear PSE, and - - - DNS. The solid gray line in (b) shows the extension of modal growth with a purely laminar spread rate. The dashed lines in (a) are extensions of the respective laminar and turbulent spread curves, intersecting at  $x_m$ : the transition location (see text). The initial thickness at the virtual origin  $x_0$  is taken as  $\delta_w|_0 = 1$ .

For an evolving mixing layer, the primary far-field sound is known to originate from sources near its transitional [23] and turbulent regions [17–21], whose positions would depend upon the streamwise spread rate  $d\delta_w/dx$  of the underlying mixing layer. The fact that a typical mixing layer evolving with a laminar spread rate [38], as obtained from the above analysis and computed within a reasonably sized computational domain, would hardly radiate much sound motivated us to include a turbulent spread rate for these initially laminar mixing layers. A typical such mean-flow spreading curve in terms of the vorticity thickness  $\delta_w$  is shown in Fig. 2(a). Here the laminar vorticity thickness follows [64]

$$\delta_l(x) \sim \sqrt{x} \quad \text{for } x < x_m, \quad (18)$$

which is immediately apparent once (4) is rewritten in terms of (15) and (16) via the computed similarity variables to yield

$$\delta_w(x) = \frac{1 - \kappa_U}{|\bar{\rho}(\eta)F''(\eta)|_{\max}} \sqrt{\frac{2x^n}{\text{Re}}}, \quad (19)$$

with  $n$  set to unity. In Eq. (19),  $\text{Re}$  is specified to be  $10^4$  for an  $M_c = 1$ , as used throughout this work, while  $\bar{\rho}(\eta)$  is just the inverse of  $\bar{T}(\eta)$ , the latter obtained from  $\bar{h}_i(\eta)$  [see (B1) in Appendix B]. The turbulent vorticity thickness  $\delta_t(x)$  is inferred via the turbulent spread rate [55]

$$\frac{d\delta_t(x)}{dx} = 0.091\phi_c \frac{(1 - \kappa_U)(1 + \sqrt{\kappa_\rho})}{1 + \kappa_U\sqrt{\kappa_\rho}} \quad \text{for } x > x_m, \quad (20)$$

where  $\phi_c = 0.5$  is the compressibility correction at  $M_c = 1$  [66], yielding  $n = 2$  in Eq. (15).

The laminar vorticity thickness curve through  $\delta_w|_0$  goes on to intersect the turbulent curve at  $x = x_m$ , so that turbulent vorticity thickness at  $x \geq x_m$  is obtained via  $\delta_t(x) = \delta_l(x_m) + (d\delta_l/dx)(x - x_m)$ , with its (constant) slope given by (20). This procedure introduces an artificial discontinuity at  $x = x_m$ , removed via a spline of width  $l_m$  about the discontinuity that smoothly blends the laminar and turbulent halves yielding the composite spread curve [e.g., Fig. 2(a)], simultaneously preserving the form of original curve to the extent possible [see (C1) for the spline equation]. Since any uncertainty over the location  $x_m$  and length  $l_m$  may carry over to the corresponding modal energy curves [see, e.g., Fig. 2(b)], in turn modifying the amount of sound radiated from the mixing layer, detailed sensitivity analyses with respect to the choice of these parameters are carried out, described briefly in Appendix C. These studies reveal (see Appendix C) that any uncertainty over  $x_m$  is indeed translated to the saturation location of respective energy curves, but in an almost proportionate

fashion, while the saturation energy magnitudes are also directly proportional to the length of the corresponding laminar growth regions. On the other hand, the apparent width of transition region, a function of  $l_m$ , when lowered allows the spline curve to be more closer to the original curve [e.g., the dashed lines in Fig. 2(a)], yielding a faster transition, which as described in Appendix C still causes a proportionate change in modal energies, without altering the respective saturation locations. Note that, within the linear modeling framework, our interest is in comparing across a set of reacting mixing layers while not making any attempt to predict their true radiated sound levels. This, coupled with a lack of available data on the growth of reacting mixing layers made us choose  $(x_m, l_m)$  after carefully studying the streamwise evolution of a set of *cold* compressible ( $M_c = 1$ ) mixing layers, with the expectation that any uncertainty over their magnitudes would not alter our conclusions, as evidenced by the sensitivity analysis of Appendix C.

Figure 2(a) shows an implementation of this composite spread curve that also contains the corresponding spreading obtained for this case from nonlinear PSE simulations [65], clearly showing the composite spread curve to roughly follow the nonlinear spread curve, of course without modeling any of the vortex pairing events of the latter. The effectiveness of this composite vorticity thickness is shown in Fig. 2(b) by tracking the streamwise energy evolution of the most unstable mode, which if evolves in a laminar mean with a laminar spread rate can grow indefinitely in an exponential fashion [linearly, when plotted in a log scale as in Fig. 2(b)], as it lacks any interaction from other modes. The mean flows of DNS and nonlinear PSE calculations include such energy exchanges, which tend to saturate these most unstable modal growths at certain streamwise distances [see Fig. 2(b)]. In spite of a purely linear approach, the composite spread curve model is clearly able to achieve similar levels of modal saturation [see Fig. 2(b)], without explicitly accounting for any nonlinear modal interactions. Such a model is expected to work even better for the supersonic cases that we consider in this work, which by itself lacks nonlinear events like vortex pairing. Note here that the chosen  $x = x_m$  location and width  $l_m$  is held constant for all the cases studied in this work (the former marked via a vertical dashed line in Figs. 4–9 below), while the turbulent portion of the spreading curves  $\delta_t(x)$  can vary via (20), yielding composite spreading curves which differ for the cases studied, with interesting consequences to the stability as discussed in Sec. III B. Once the spreading curve  $\delta_w(x)$  for the mixing layer is fixed at each of the streamwise locations, the mean profiles  $\bar{q}(x, y)$  are computed by transforming  $\bar{q}(\eta)$  to the physical space via (19), (15), and (16). Finally, note that initial vorticity thickness  $\delta_w|_0 = 1$  provides the location of the virtual origin  $x_0$  via (19) (see also Fig. 2), and all streamwise distances reported here have this distance subtracted out.

### C. Aeroacoustic source model

In a *direct* method, as followed here, the radiated sound waves are directly computed from the reduced governing equations (8), which however, do not provide any description of the sound sources. Instead, we use the Lilley-Goldstein equation [23,67], which models aeroacoustic sources in parallel, transversely sheared flow, where the source term  $\Gamma$  is composed of a quadrupole velocity and a dipole temperature component

$$\bar{L}_0 \pi = \Gamma = \frac{D_0}{Dt} \frac{\partial f_i}{\partial x_i} - 2 \frac{\partial \bar{u}}{\partial x_j} \frac{\partial f_j}{\partial x_1}, \quad (21)$$

where  $f_i$  is akin to an externally applied force

$$f_i = -\frac{\partial}{\partial x_j} (1 + \pi) \hat{u}_j \hat{u}_i - \hat{T} \frac{\partial \pi}{\partial x_i}, \quad (22)$$

with  $D_0/Dt \equiv \partial/\partial t + \bar{u} \partial/\partial x_1$ , the pressure  $\pi = (p/\hat{p})^{1/\gamma} - 1$ , and  $\bar{L}_0$  is the third-order Pridmore-Brown operator [67].

In this work, the source terms in Eq. (21) are computed from PSE solutions of Sec. II A, which are not further solved for the radiated sound, since for supersonic shear layers, the instability wave-based PSE model is sufficient in providing a complete representation of the far-field aeroacoustics. Instead



in Sec. III, we use the source models provided by (21) to understand how well the locations and magnitudes of the peak sources correlate with their radiated sound.

#### D. Boundary and initial conditions

The calculation of modes that are supersonic relative to at least one of the free streams ( $\bar{M}_{n,k} > 1$ ) require an implicit approach while specifying the conditions at the supersonic side [38]. This is due to the fact that these modes show an oscillatory decay as they approach the particular boundary, which is not modeled by the typical homogeneous Dirichlet boundary conditions [68], otherwise applied to the boundary where the phase speed is subsonic. In this work, the following boundary conditions are used:

$$\begin{aligned} \frac{d\tilde{q}_n}{dy} &= \mp\lambda \tilde{q}_n \quad \text{as } y \rightarrow \pm\infty \quad \text{for } \bar{M}_{n,k} > 1, \\ \tilde{q}_n &= 0 \quad \text{as } y \rightarrow \pm\infty \quad \text{for } \bar{M}_{n,k} < 1, \end{aligned} \quad (23)$$

with  $k \equiv 1, 2$ . Here  $\lambda$  is the complex coefficient of an exponential decay function obtained from linear stability analysis [38].

Initial conditions  $(\tilde{q}_n, \alpha_n)|_{x_0}$  for solving (8) are obtained by solving a parallel-flow version of (5) using the calculated mean at that location. The governing equations are combined to obtain a single Rayleigh-type stability equation which is then solved using a shooting method satisfying the appropriate boundary conditions [69].

#### E. Numerical methods

The PSEs (8) are discretized using fourth-order central differences in the  $y$  direction and first-order implicit Euler differences for the streamwise derivatives. The derivative in the boundary term (23) is computed to a first-order difference. This yields a system of equations to be solved for the shape functions  $\tilde{q}_n$  at each of the streamwise locations, where parabolization implies some restrictions on the step size  $\Delta x$  [70]. The wave number is updated at each step using an iteration-based normalization condition of the shape function [16,61]:

$$\alpha_{j+1}^{k+1} = \alpha_{j+1}^k - \frac{i}{\Delta x} \frac{\int_0^\infty (\tilde{q}_{j+1}^k)^* (\tilde{q}_{j+1}^k - \tilde{q}_j^k) dy}{\int_0^\infty |\tilde{q}_{j+1}^k|^2 dy}, \quad (24)$$

where  $()^*$  denotes complex conjugate,  $j$  is the streamwise step index, and  $k$  the iteration step index. Only the velocity components are used in Eq. (24) to obtain convergence of  $\alpha_n$  within  $10^{-9}$ , which then yields the shape functions.

### III. AEROACOUSTIC SOURCES AND RADIATED SOUND

#### A. Modal classification

Compressible, reacting mixing layers potentially contain additional unstable modes over the incompressible, central (K-H) mode [38,48,49,62,71], but unless the relative Mach number  $\bar{M}_{n,k} > 1$  for any unstable mode  $\omega_n$  in at least one of the streams  $k = 1, 2$ , these are unimportant from the point of radiating sound via Mach waves. The modal classification we employ follows this requirement, where a mode  $\omega_n$  is classified as a “fast” mode if it radiates toward the slow side ( $y \rightarrow -\infty$ ) of the mixing layer with  $\bar{M}_{n,1} < 1$  and  $\bar{M}_{n,2} > 1$  [e.g., Fig. 3(a)], while a “slow” mode radiates to the fast side ( $y \rightarrow \infty$ ) with  $\bar{M}_{n,1} > 1$  and  $\bar{M}_{n,2} < 1$  [e.g., Fig. 3(b)] [38,49]. A central mode is either of subsonic speed in both streams ( $\bar{M}_{n,k} < 1$  for  $k = 1, 2$ ) or supersonic in both. In the former case, no Mach wave radiation is possible (e.g., the case K00 in Table I) since the instability wave model fails to couple with the far-field sound, which instead radiates sound via a vortex-pairing mechanism that generates higher harmonics by means of nonlinear interactions [23], beyond the scope of the present

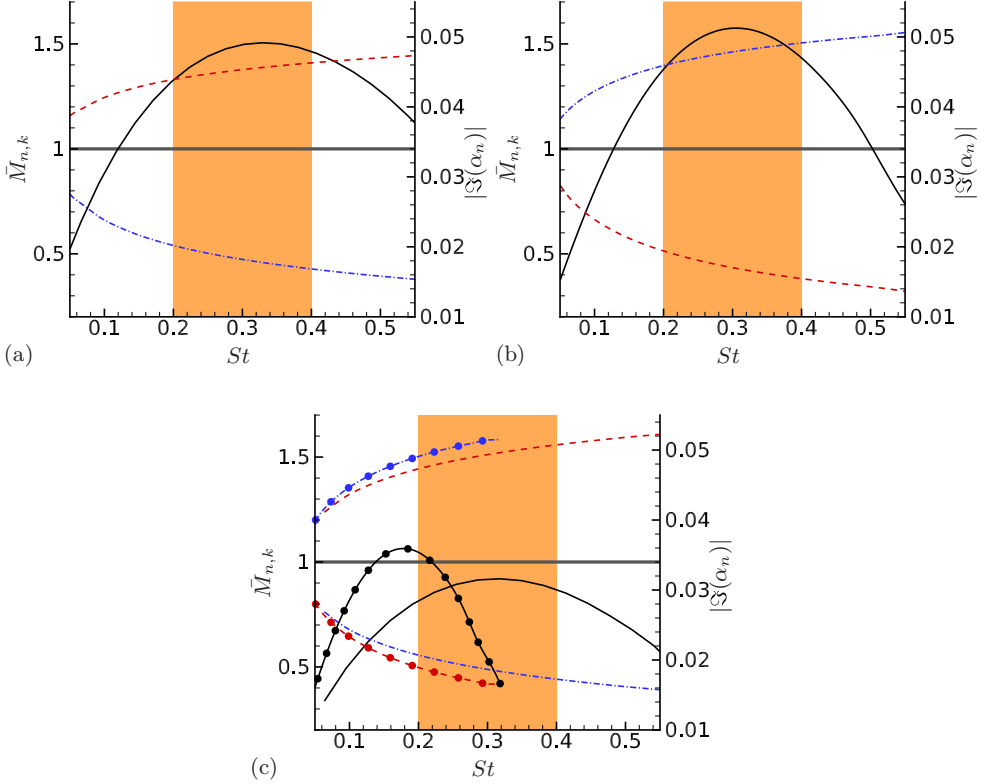


FIG. 3. Relative Mach numbers  $\cdots\cdots\bar{M}_{n,1}$ ,  $\cdots\bar{M}_{n,2}$ , and modal growth rates  $\text{---} |Z(\alpha_n)|$  as a function of Strouhal number  $St$  shown for (a) F1010, (b) S1010, and (c) C1010 cases of Table I. In case (c), the lines with symbols indicate the slow mode. The shaded box is the extent of broadband spectra considered in this work, while a thick horizontal line marks  $\bar{M}_{n,k} = 1$ .

linear model. The other case, where the central mode can potentially radiate to both sides of the mixing layer, is possible only for appropriately large  $M_c$ , when the K-H mode is largely stabilized and has little influence on the far field, similar to what has been observed for highly compressible free jets [56].

The listed cases in Table I include the three possible scenarios that may arise out of the fast and slow modes in a broadband source perturbed at three discrete frequencies of  $St = 0.2, 0.3$ , and  $0.4$ , where the Strouhal number  $St = \omega \delta_w |_0 / 2\pi(1 - \kappa_U)$ . A fast case (prefixed by an ‘‘F’’ in Table I) is one where the most unstable modes at all the discrete frequencies are of fast types, in a slow case (prefixed by ‘‘S’’) they are all of slow types, while a colayer case (prefixed by ‘‘C’’) has a mixture of most unstable fast and slow modes as shown in Fig. 3(c) for the  $\Theta = 1$  and  $\phi = 1$  baseline colayer case. To study the effect of heat release and chemical composition (via  $\Theta$  and  $\phi$ , respectively) on these broadband sources, these baseline configurations are varied to yield all the different cases of Table I. In practical configurations, the effective heat release from diluted fuel or oxidizer streams like we consider here [see (3)] is expected to be limited [57], restricting  $\Theta = 1.5$  at the maximum, sufficient for drawing useful conclusions within a linear framework. To simplify matters, we follow a naming convention where the first two digits immediately following the type-identifying letter prefix indicate the heat-release parameter  $\Theta$ , while the last two digits indicate the equivalence ratio  $\phi$ . A cold central mode ‘‘K’’ case is also considered at the frequency of its maximum growth rate to serve as a benchmark for the outer mode cases. Note that the specific choice of broadband spectrum follows from the observation that the most unstable mode for the cases considered in Table I falls within the  $St = 0.2\text{--}0.4$  range (except C1010 and C1015, both of which are marginally outside at

LINEAR MODELS FOR SOUND FROM SUPERSONIC ...

TABLE I. A summary of the cases presented with  $M_c = 1$  and  $M_1 = 4$  held constant.  $\bar{\rho}\partial\bar{u}/\partial y$  is plotted for  $y \in [-1.6, 1.3]$  and the peak for K00 case is at 0.417. The unit of  $\text{SPL}_{\max}$  is dB and  $\theta_{\max}$  (at  $r = 270$ ) is in degrees.

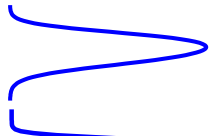
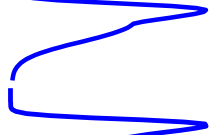



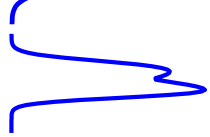
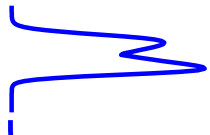

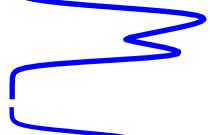

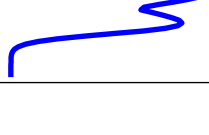

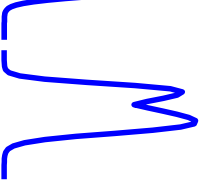
Cases	$\bar{\rho}\partial\bar{u}/\partial y$	$\kappa_\rho$	$\Theta$	$\phi$	$ \Gamma _{\max} \times 10^4$	$(x, y) _{\Gamma_{\max}}$	$\text{SPL}_{\max}$	$\theta_{\max}$
K00		1.0	0.0	-	1889	(187,0)	-	-
F0510		0.5	0.5	1.0	94	(191,0.95)	-20.23	-11.05
F1010		0.5	1.0	1.0	678	(192,1.15)	-17.66	-11.30
F1510		0.5	1.5	1.0	2734	(200,1.29)	-16.61	-11.15
F1005		0.5	1.0	0.5	697	(213,1.15)	-17.36	-11.20
F1015		0.5	1.0	1.5	481	(161,0.68)	-19.19	-11.40
S0510		1.5	0.5	1.0	1578	(210,-0.88)	-21.14	4.15
S1010		1.5	1.0	1.0	2836	(225,-1.15)	-12.90	3.60
S1510		1.5	1.5	1.0	69936	(229,-1.29)	-8.66	3.05
S1005		1.5	1.0	0.5	194	(226,-0.95)	-21.74	3.95
S1015		1.5	1.0	1.5	2304	(221,-0.95)	-12.79	4.30
C1010		1.0	1.0	1.0	23	(148,0.68)	-24.45	-7.85

TABLE I. (Continued.)

Cases	$\bar{\rho}\partial\bar{u}/\partial y$	$\kappa_\rho$	$\Theta$	$\phi$	$ \Gamma _{\max} \times 10^4$	$(x, y) _{\Gamma_{\max}}$	SPL <sub>max</sub>	$\theta_{\max}$
C1510		1.0	1.5	1.0	88	(172, -0.81)	-21.67	5.90
C1015		1.0	1.0	1.5	15	(139, 0.68)	-26.42	6.60

$St \approx 0.18$ ) (see also the case in Fig. 3), which ensures the most unstable frequency to be always contained within this spectrum. For the colayer case in Fig. 3(c), the fast mode takes over the role as the most unstable mode beyond  $St \gtrsim 0.25$ , which ensures a broadband perturbation that includes both slow and fast modes. In all the cases, we have fixed  $M_c = 1$  and  $M_1 = 4$  while the density ratio  $\kappa_\rho$  is varied to alter the density-weighted vorticity  $\bar{\rho}\partial\bar{u}/\partial y$ , yielding the necessary biased modal configurations, as illustrated inside Table I. Note that the velocity ratio  $\kappa_U$  is directly related to  $\kappa_\rho$  via  $\kappa_U = 1 - (M_c/M_1)(1 + 1/\sqrt{\kappa_\rho})$ , once the Mach numbers are fixed. The spanwise wave number  $\beta = 0$  for all the cases except the cold central mode K00, a three-dimensional mode with a peak at  $\beta = 0.5$ .

The far-field sound is computed at an arc of radius  $r = 270$ , fixed at the splitter end (see Fig. 1), with  $\theta$  measured from the downstream direction. This distance is chosen to lie well within the acoustic far field, when considering the wavelength of the longest possible acoustic wave supported by our computations.

### B. Fast and slow cases

With  $M_c$  and  $M_1$  held constants, a bias in mean density yields the fast and slow modes, where the side with the larger density produces a sharper local peak in the corresponding mean-density-weighted vorticity ( $\bar{\rho}\partial\bar{u}/\partial y$ ) profiles as can be seen from Table I. Unlike in the central-mode dominated case K00 (with  $\kappa_\rho = 1$ ), this density bias introduces new vortical structures that are offset from the K-H mode location and near the local peaks of  $\bar{\rho}\partial\bar{u}/\partial y$ .

Figure 4 shows the Lilley-Goldstein source  $|\Gamma|$  superimposed upon the total pressure contours for the case K00. Note that unlike the broadband outer mode cases to follow, the K00 case is composed of just the most unstable mode at  $St = 0.08$  and  $\beta = 0.5$ . This lower tonal perturbation frequency is immediately apparent from the longer-wavelength pressure contours, showing a typical wave-packet-like shape. Its subsonic phase speed implies fast decay outside the hydrodynamic near field (see also Figs. 6, 7, and 9 where the K00 case is compared to outer mode cases), whereas the source fluctuations appear over a much compact region near the flow interface.

The near-field source and pressure contours of the fast and slow cases of Table I are shown in Fig. 5, whereas Figs. 6 and 7 plot the near-field modal evolution and the far-field sound for these fast and slow cases, respectively. As expected, in these figures most of the sound source fluctuations (colored contours) are seen to originate downstream of the transition location  $x_m = 120$ , which along with  $l_m = 120$  is imposed on the composite spread model of the mixing layer, as discussed in Sec. II B. Although, the peak sources in Fig. 5 seem to be located significantly further downstream of  $x = x_m$ , perhaps pointing to the relatively slow growth of these mixing layers. The streamwise evolution of instability modes in the near field is tracked via an integrated energy measure [72]

$$\hat{E}(x) = \sum_n \int_{-\Upsilon}^{\Upsilon} \left\{ \bar{\rho}(|\hat{u}_n(x, y)|^2 + |\hat{v}_n(x, y)|^2) + \frac{\bar{T}|\hat{\rho}_n(x, y)|^2}{\bar{\rho}} + \frac{\bar{\rho}|\hat{T}_n(x, y)|^2}{\bar{T}} \right\} dy, \quad (25)$$

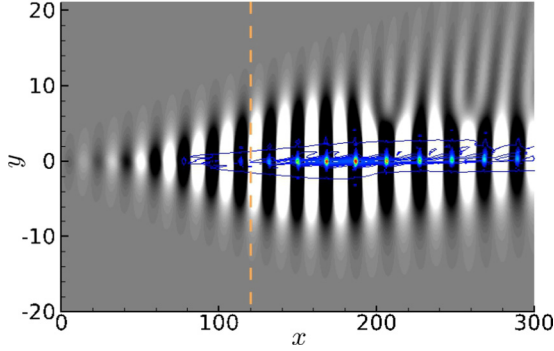


FIG. 4. Colored contours of the Lilley-Goldstein source  $|\Gamma|$  of (21) superimposed on the real part of total pressure contours in gray scale, shown here for the K00 case of Table I. The vertical dashed line is the location of transition point  $x_m$  in the composite spread curve used (see Sec. II B). There are 30 pressure contour levels in between  $\pm 0.003$  and 100 source contours in between  $10^{-4}$  and 0.16.

where the eigenfunctions are according to (7),  $y = \pm \Upsilon$  are the hydrodynamic near-field cutoff points, and the sum is over  $St = 0.2, 0.3$ , and  $0.4$  ( $n = 3$ ).

In general, the slow-mode-dominated cases show a faster streamwise growth of the integrated energy ( $d\hat{E}(x)/dx$ ) than the fast modes, yielding higher magnitudes of the respective source fluctuations, further leading to louder sound radiations at shallower angles. This may be understood from the fact that slow mode cases have slower turbulent spread rates of  $d\delta_t(x)/dx$  [see Eqs. (20) and (26) below] than the fast cases of Table I, yielding lower mixing layer thicknesses, thus expected to yield modal growth rates higher than the corresponding fast cases. This also follows from the well-known effect a finite-thickness mixing layer has on the growth of K-H central mode, which for a given perturbation frequency is known to slow down on increasing thickness [73]. In order to explain the slower spread rates of the slow cases, first note that, although such spread rates of compressible mixing layers are known to be well-correlated with  $M_c$ , at higher values of the latter additional dissipation due to the temperature ratio ( $\kappa_\rho$  in our case) of the streams becomes prevalent [74]. Next, once  $M_c$  and  $M_1$  are held constants, (20) yields

$$\frac{d\delta_t(x)}{dx} = \Re\left(1 + \frac{1}{\kappa_\rho}\right), \quad (26)$$

where  $\Re$  is a function of  $M_c$  and  $M_1$ . Equation (26) clearly points to lower spread rates of the slow mode cases which have higher  $\kappa_\rho$ , as per Table I. Specifically for the parameters listed in Table I,  $d\delta_t(x)/dx|_{\text{slow}} = 2.75 \times 10^{-2}$  whereas  $d\delta_t(x)/dx|_{\text{fast}} = 3.66 \times 10^{-2}$ , implying the fast cases to be more than 30% faster spreading. The same is also reflected in the source contours of Fig. 5, where greater spread of the sound sources in fast cases point to thicker mixing layers.

### 1. Effect of heat release

The heat release parameter  $\Theta$  varies between the cases in Figs. 5(a), 5(c), and 5(e) which are shown together in Figs. 6(a) and 6(c) for the fast mode cases and between Figs. 5(b), 5(d), and 5(f) and shown in Figs. 7(a) and 7(c) for the corresponding slow mode cases. On comparing Figs. 6(a) and 7(a), it is easy to note the more pronounced effect that  $\Theta$  has on the growth rates of the more unstable slow mode cases, where the S1510 case [see Fig. 7(a)] attains the highest modal growth among all the cases considered here, easily exceeding the central K00 case by a few orders of magnitude. For the slow (or fast) cases, the turbulent spread rate of (20) depends upon the ratios of free stream parameters, which remain unchanged, but as  $\Theta$  is raised additional energy is available via increased heat of formation [see (13) and (14)], which results in a steeper mean temperature (or

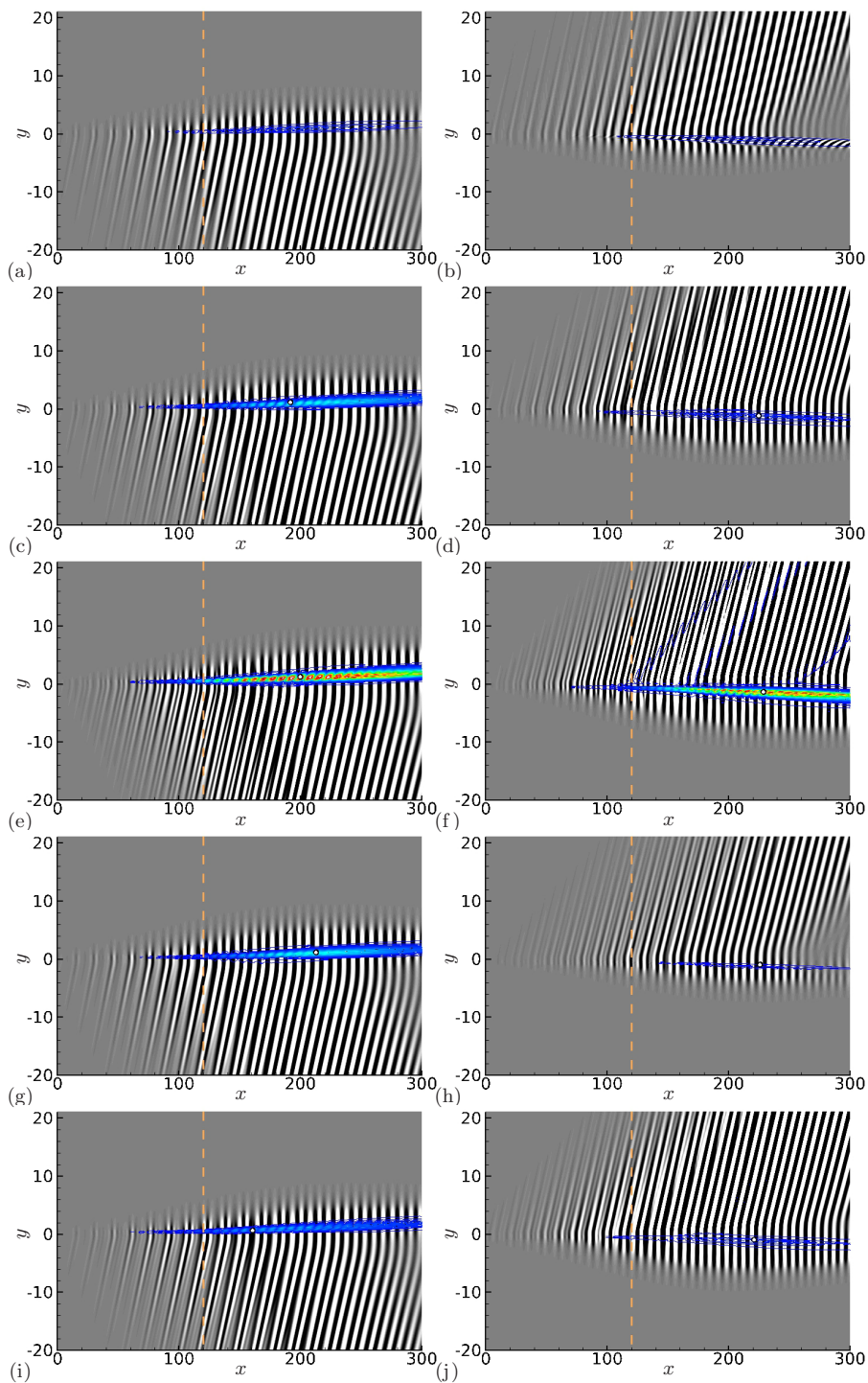


FIG. 5. Same as in Fig. 4 for the following cases: (a), (c), (e), (g), and (i) F0510–F1015 (left column) and (b), (d), (f), (h), and (j) S0510–S1015, all in the order of being listed in Table I. The filled white circle inside the source in some of the cases indicate the location of  $|\Gamma|_{\max}$ . Here the source contours are in between  $8 \times 10^{-4} - 0.18$  for the fast mode cases and  $5 \times 10^{-3} - 5.5$  for the slow mode cases.

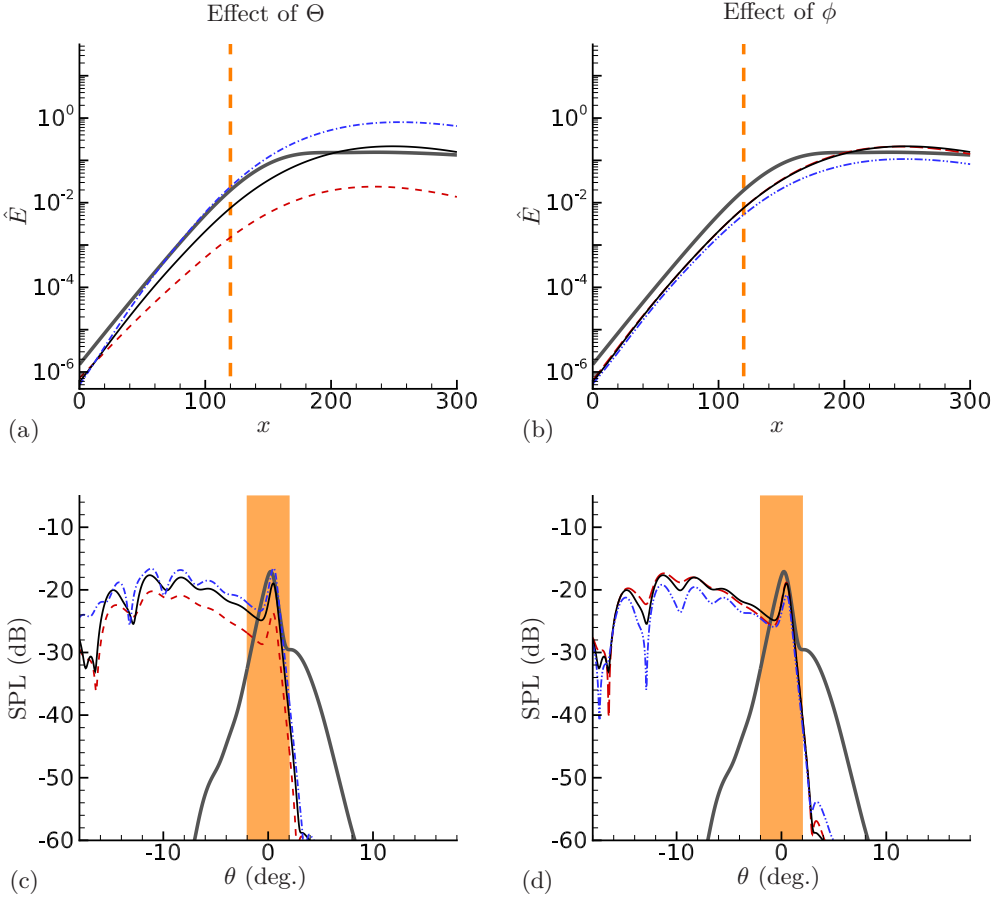


FIG. 6. The integrated modal energy of (25) are plotted in (a) and (b) with the corresponding sound pressure levels (SPL) in dB, shown in (c) and (d) for — F1010; --- F0510; - · - · - F1510; — — — F1005; and - · - · - · - F1015 cases of Table I. Case K00 is shown by the thicker gray line, while the vertical dashed line is the location of transition point  $x_m$  in the composite spread curve (see Sec. II B). The shaded box spanning  $\pm 2$  degrees in the SPL plots corresponds to  $\Upsilon = 9.4$  in Eq. (25), representing the estimated zone of influence of near-field hydrodynamics.

density) gradient inside the mixing layer. This may also be noticed from Table I, where as  $\Theta$  is raised, the corresponding  $\bar{\rho} \partial \bar{u} / \partial y$  profiles seem to possess increasingly pronounced peaks, although their magnitudes drop. The latter infers the lower  $\Theta$  cases to be more unstable near to the splitter, which is where the  $\bar{\rho} \partial \bar{u} / \partial y$  profiles of Table I are calculated. However, the higher  $\Theta$  cases with their sharper peaks grow faster, quickly assuming dominance at relatively shorter distances ( $x \sim 10$ ) downstream of the splitter. Increased temperature gradients thus lead to higher sound source fluctuations, further amplified for the slow cases, which have relatively lower spreads of the mixing layer (see also the  $|\Gamma|_{\max}$  values in Table I). The locations of the peak sources shift to further downstream (and deeper inside the fast or slow side) as  $\Theta$  is raised (check the corresponding peak source locations in Fig. 5), apparently due to the extra diffusive processes in reacting mixing layers at higher heat release that push the flame sheet and the source fluctuations away.

Both slow and fast modes radiate efficiently as Mach waves into the stream of supersonic phase speed, quantified by their relative Mach numbers [see (9)], as shown in Fig. 3 for a few example cases. The angle at which these Mach waves radiate is a function of  $\bar{M}_{n,k}$  via  $\hat{\theta}_n = \pi - \cos^{-1}(1/\bar{M}_{n,k})$  [75].

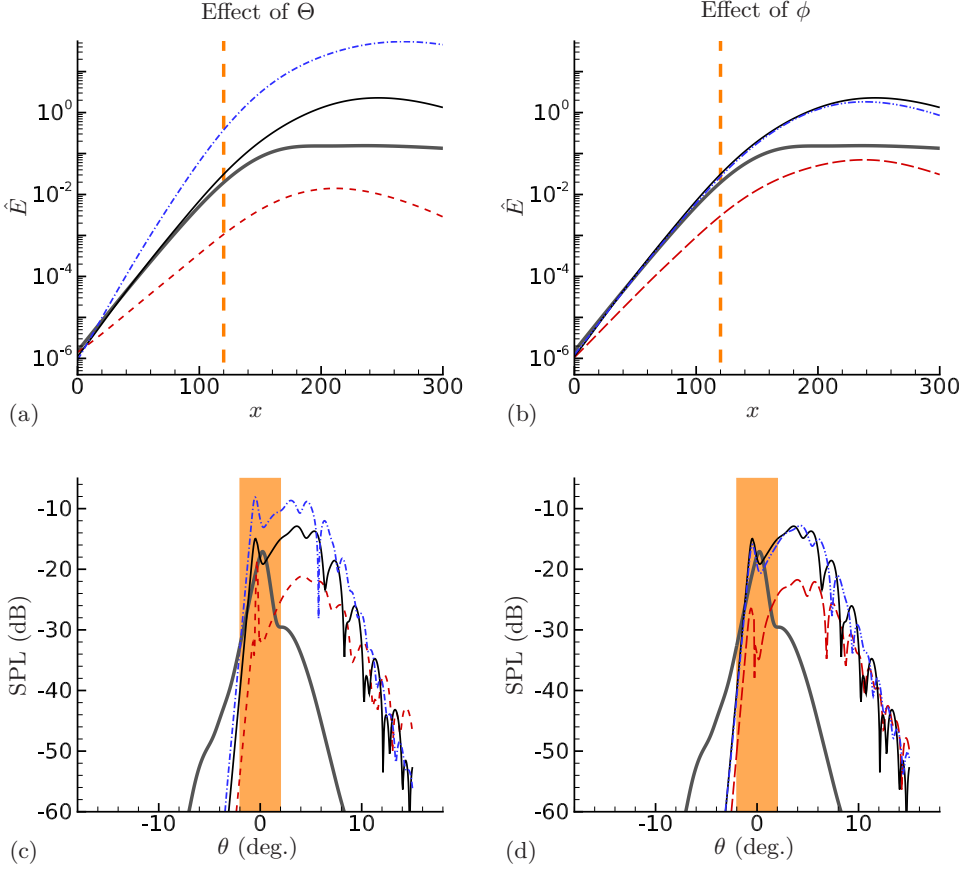


FIG. 7. Same as in Fig. 6 for — S1010; --- S0510; - · - · - S1510; — — — S1005; and - - - - - S1015 cases of Table I.

In general, slow mode cases have higher supersonic relative Mach numbers in the fast stream  $\bar{M}_{n,1}$  than the relative Mach numbers of the fast modes in the slow stream  $\bar{M}_{n,2}$  (see also Fig. 3), ensuring the slow mode cases to radiate at shallower angles (see Table I) than the corresponding fast cases. Further, as  $\Theta$  increases, these broadband sources radiate at even shallower angles, clearly evident for the first three slow cases of Table I. Note that unlike the slow modes, the fast cases shown in Figs. 6(c) and 6(d) radiate over a relatively broad range of angles, as a true broadband source should, because of the fact that component modes ( $St = 0.2\text{--}0.4$ ) in the fast cases grow over longer streamwise distances, yielding sources that are more distributed (compare the respective source structures in Fig. 5). In the slow cases, sources are more compact, yielding far-field spectra peaking within a narrow range of angles [Figs. 7(c) and 7(d)]. The peak sound levels at these angles depend directly on the corresponding  $|\Gamma|_{\max}$  magnitudes, as a linear theory would suggest. In our analysis of the far-field, we neglect any peak if it appears within the shaded band of Figs. 6(c) and 6(d) or Figs. 7(c) and 7(d), which would then correspond to hydrodynamic fluctuations.

## 2. Effect of equivalence ratio

The effect of  $\phi$  on the dynamics of fast and slow modes is more interesting, whose individual field plots are shown in Figs. 5(c), 5(g), and 5(i), while the modal evolutions and far-fields are together in Figs. 6(b) and 6(d), respectively, for the fast cases and similarly in Figs. 5(d), 5(h), and 5(j) and in Figs. 7(b) and 7(d) for the slow cases. As discussed in Sec. I, with the increased use of lean ratios



in commercial turbine engines, the effect that varying  $\phi$  has on the near-field flow dynamics and its radiated sound has assumed significance. Although the role of  $\phi$  on the aeroacoustic characteristics of reacting flows has been anticipated [7], most of the previous studies have focused on either premixed or partially premixed configurations [76–79]. In the model nonpremixed configuration as considered here,  $\phi$  may modulate the mean profiles via changing the heat of formation as given by (13) and (14). However, with all other factors held constant,  $q_c^*$  is proportional to  $(1 + 1/\phi)$  via (12), where  $Y_{O,\infty}$  and  $n$  are fixed with respect to a given chemical process as per (3). This ensures a greater increase in the heat of formations for leaner ratios  $\phi < 1$  than a comparatively smaller decrease at richer mixtures  $\phi > 1$  [via (12)], if  $\phi$  is varied by the same amount about the stoichiometric ratio, as we do here.

The effect of this variation on the slow- and fast-mode-dominated cases is quite different. For the fast mode cases of Fig. 6(b), the differences in the respective  $\hat{E}$  across varying  $\phi$  are minimal, which in contrast is more significant for the slow mode cases of Fig. 7(b). This may be explained on revisiting the individual  $\bar{\rho}\partial\bar{u}/\partial y$  profiles of Table I. When the mixture is lean ( $\phi = 0.5$ ), the flame sheet moves to the slow (fuel) side with a minima in  $\bar{\rho}$  located somewhere below  $y = 0$ , which for the slow mode case S1005 directly acts against the peak in  $\partial\bar{u}/\partial y$ . Because the lean cases have mean density minimas that are lower than the corresponding rich cases, the resulting effect is a  $\bar{\rho}\partial\bar{u}/\partial y$  profile with a considerably reduced slow-side peak, yielding a weaker slow mode [see Fig. 7(b)]. In fact, there is a stronger fast-side peak in  $\bar{\rho}\partial\bar{u}/\partial y$  (at  $x = 0$ ) for this case, which decays to be negligible, starting from  $x \sim 10$ . In contrast, the effect of this lean parametric configuration on the fast mode case F1005 is minimal when compared to the  $\phi = 1$  case (F1010) [the corresponding curves in Fig. 6(b) are almost indistinguishable] as the  $\partial\bar{u}/\partial y$  peak is now on the other (fast) side.

In contrast, the rich  $\phi = 1.5$  mixture is unable to modulate the fast F1015 case (when compared to the F1010 case) in any appreciable manner [see Fig. 6(b)] as their respective heat of formations are not significantly different. In fact, even a theoretically infinite rich case  $\phi \rightarrow \infty$  changes the heat of formation to only one-half of the stoichiometric conditions.

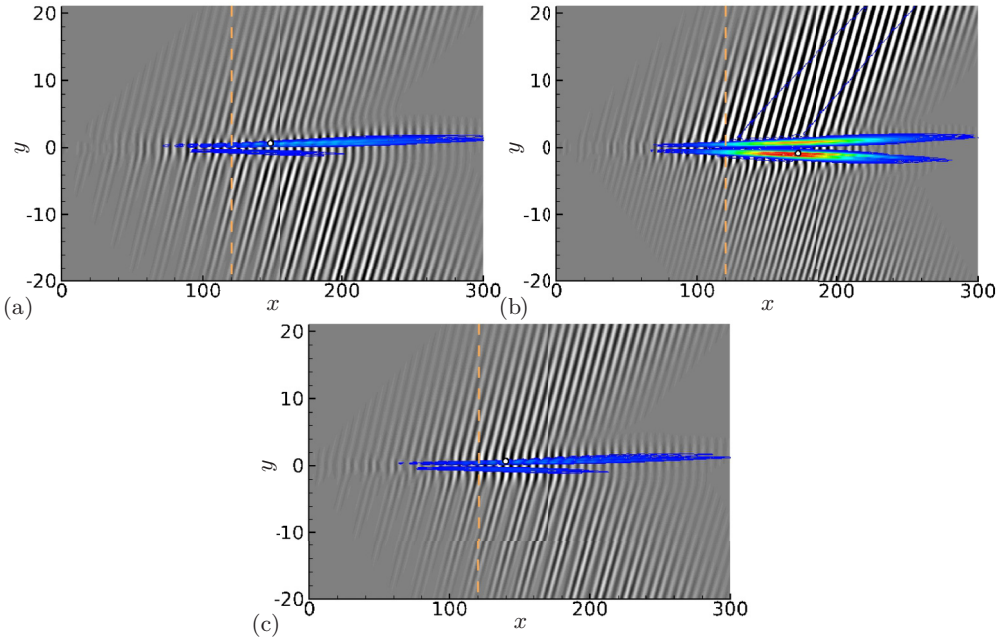


FIG. 8. Same as in Fig. 4 for the following cases: (a)–(c) C1010 – C1015, in order of Table I. The source contours have 100 steps in between  $1.2 \times 10^{-4}$  –  $7.5 \times 10^{-3}$ .

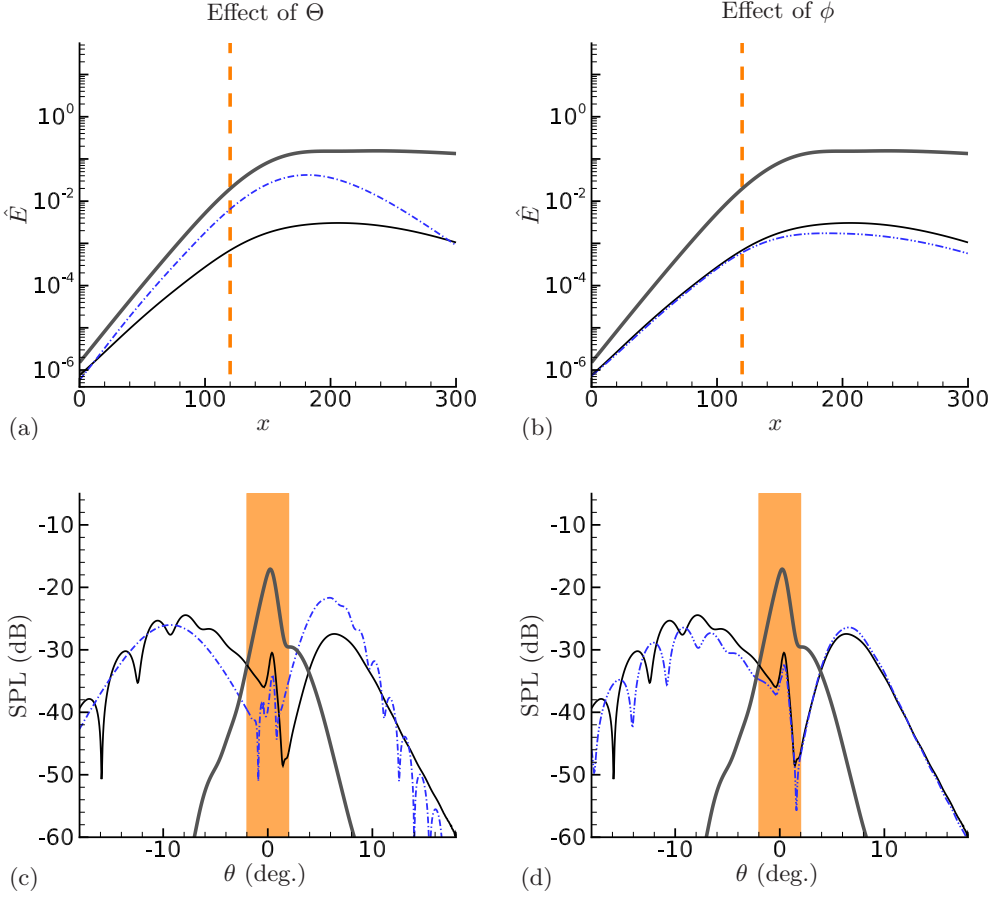


FIG. 9. Same as in Fig. 6 for — C1010; - · - · - C1510; and - · - · - C1015 cases of Table I.

The SPL levels of Figs. 6(d) and 7(d) follow the near-field fluctuations, where the lean slow case S1005 is easily the quietest flow (see also Table I). The lean cases F1005 and S1005 radiate at shallower angles than the corresponding rich cases as the respective peak source locations for these cases are at further downstream (see Table I and Fig. 5).

### C. Colayer cases

A colayer case is one where the instability structures may radiate to either side of the mixing layer, and in this way these cases are intermediate to the fast and slow cases of Table I. However, do note that unlike in Day *et al.* [38], whose colayer cases are located right at the regime boundaries with equal growth rates of slow and fast modes, we use a slightly different definition in this work. We label a case to be of colayer type, if within a given broadband mix ( $St = 0.2-0.4$  in our case), a different type of mode is dominant in at least one of the discrete frequencies. Using this definition, a broadband spectrum containing *all* the frequencies will perhaps be of colayer type in any parametric configuration. In fact, had we included a wider range of frequencies in our broadband mix, many of the fast and slow cases of Table I would turn to colayer type. Note that in Table I, cases C0510 and C1005 are absent, since at these parametric conditions the corresponding fast modes dominate over the entire chosen broadband range, so these cases are rather of fast type.

All the colayer cases shown in Figs. 8 and 9 are less unstable than all the fast and slow cases of Table I. On comparing we note that even the C1510 case is more hydrodynamically stable than the

lower heat release F0510 case, with the former radiating lesser sound as expected. The source terms in these cases have branches on both the slow and fast sides (see Fig. 8) with the most unstable branch usually deciding the side of dominant radiation. For example, in the C1510 case of Fig. 8(b), the branch on the slow side is clearly more unstable, yielding a dominant radiation resembling the slow mode cases of Table I. The source fluctuations for these mixed-mode colayer cases peak at distances that are considerably upstream (and closer to the layer interface) than the single outer-mode dominated cases.

The peak radiation angles for the colayer cases are between those of the fast and slow cases (see Table I). Curiously, for the C1015 case the peak radiation appears to be on the fast side, where it is also more hydrodynamically unstable. This may be resolved from Fig. 9(d), where it is easy to see that although the respective radiation peaks are of similar amplitudes on both sides, the multilobe pattern characteristic of broadband radiation appears only on the slow side, which is indeed the direction of its primary radiation.

#### IV. CONCLUSIONS

Although the importance of outer modes on the dynamics of reacting shear flows has long been anticipated [38,50,52], to date the configurations studied in the experiments and numerical simulations have largely revolved around the central K-H mode. In this work, a set of supersonic mixing layers are studied at higher heat release conditions (i.e., higher  $\Theta$ ), when some of the two-dimensional outer modes dominate over the three-dimensional central mode of an equivalent cold mixing layer. The main focus has been on quantifying the nature of near-field instabilities and the associated Mach radiation as density ratio  $\kappa_\rho$ , heat release parameter  $\Theta$ , and equivalence ratio  $\phi$  are systematically varied for a fixed amount of compressibility  $M_c$ . In this context, we note here briefly that although the wave packet nature of the near-field pressure were visible in the respective field plots (see Figs. 4, 5 and 8), this has not been further pursued in this work, whose analysis in itself could be an interesting future exercise.

A composite spread curve has been used for the mean evolution of the mixing layers which indirectly introduced flow nonlinearities via inclusion of a turbulent region. In the absence of any useful documented data on the spreading of reacting mixing layers, the estimate of transition location in our spreading model has been based on cold, compressible layers. In future, as data on reacting mixing layers become available, this composite spread model may be recalibrated, which perhaps would yield a more direct validation of the model. In any case, the success of linear PSE in tracking the modal evolution using such a spreading model that favorably compares to the more computationally expensive nonlinear calculations (shown here for a nonreacting case) supports the recent claim that linearized fluctuations evolving on a turbulent base flow are enough to correctly capture large-scale structures in shear flows [41].

Once the compressibility is fixed,  $\kappa_\rho$  modulates the nature of instabilities via biasing the density in one of the streams of the mixing layer, yielding the outer-mode-dominated regimes in our work. The slow mode cases, when the major instabilities are confined within the fuel side, are found to be more unstable and sensitive to parametric changes. These cases have relatively thinner mixing layers with lower spread rates which are more susceptible to perturbations. The corresponding aeroacoustic sources are more compact and found to radiate at shallower angles. The fast mode cases with thicker shear layers are significantly less unstable, and these are less likely to exceed the central mode instability even when  $\Theta$  is raised significantly.

For all the cases studied, increased heat release yielded higher levels of instability and sound. This is in stark contrast to the expectations from a K-H central mode where higher heat release weakens both the streamwise and spanwise vortical structures at the core of the mixing layer, thus attenuating its growth. The outer modes, on the other hand, are fully compressible and depend on the location of flame surface (via heat release parameter) and the associated shear between this flame and free stream. As  $\Theta$  is raised, the flame sheet is pushed further away from the mixing layer core

for both the slow and fast cases, thereby raising shear and a steeper gradient in the density-weighted vorticity, yielding greater potential for modal instabilities.

The variation of equivalence ratio, usually thought to be of lesser importance in flow dynamics, yielded interesting conclusions. The fast modes are found to be mostly unaffected by moderate changes of equivalence ratios about the stoichiometric  $\phi = 1$  mixture. In contrast, even in moderately lean mixtures the corresponding slow mode is found to be noticeably stabilizing, once the flame sheet is located closer to the maximum change in mean velocity, via a reduction of the density-weighted vorticity production.

### ACKNOWLEDGMENT

Partial support for this work has been provided by the Aeronautical Research & Development Board (ARDB), Government of India via Grant No. DARO/08/1031709/M/I.

### APPENDIX A: VALIDATION

The linear PSE algorithm used in this work has been extensively validated against other mixing layer simulations, both subsonic and supersonic [23,38], the details of which appear elsewhere [69]. Here we briefly compare the results of the present linear PSE solver for a cold supersonic mixing layer with its DNS results reported in Cheung and Lele [23] for their case M29M1, as shown in Fig. 10. The spanwise vorticity contours obtained from the linear PSE shown in Fig. 10(b) are remarkably similar to the DNS of Fig. 10(a), which reaffirms the excellent ability of linear models in capturing the large-scale structures of supersonic mixing layers. Such mixing layers lack vortex pairing in the near field, a nonlinear process, owing to an absence of the subharmonic frequencies [23], which makes them amenable to such linear models. The integrated modal energy of (25) is shown in Fig. 10(c), where beyond  $x > 100$ , as plotted, the linear PSE starts over predicting the DNS results when apparently the lack of (nonlinear) intermodal interactions in the former starts showing up in the modal evolution. However, note that a nonlinear PSE model which includes these interactions does not seem to fare any better in Fig. 10(c). In spite of these differences in the near-field modal evolution, the location and amplitude of the peak Mach radiation as obtained from the linear PSE match very well with the DNS as shown in Fig. 10(d), where the respective peaks are off by a mere 2 dB. The far-field predictions from the nonlinear PSE calculations are almost indistinguishable from our linear PSE model at these angles.

### APPENDIX B: MEAN FLOW COMPUTATIONS

The similarity equations (17) for the laminar mean along with the appropriate boundary conditions [38,69] are solved using a shooting method with a dual iteration [65,69,80] to first correctly obtain  $F(\eta)$  from the first similarity equation. The second and third equations are then solved for  $\bar{Z}(\eta)$  and  $\bar{h}_t(\eta)$ . The latter yields the mean temperature, obtained via

$$\bar{T}(\eta) = [\bar{h}_t(\eta) - \bar{Y}_F(\eta)h_{f,F}^* - \bar{u}^2(\eta)/2]/c_{p1}, \quad (\text{B1})$$

after subtracting out the chemical and kinetic energies. The mean profiles so obtained are shown here for the cases F1010 and S1010 of Table I in Fig. 11. The differing  $\kappa_\rho$  in these two cases introduce changes in  $\bar{u}$  and  $\bar{T}$  while  $\bar{Z}$  remains unchanged (as  $\phi = 1$ ). The flame sheets are located by the respective peak in mean densities (or temperatures in Fig. 11), which along with the shear in  $\bar{u}$  yield the  $\bar{\rho}\partial\bar{u}/\partial y$  profiles, at the heart of origin of outer modes, illustrated in Table I.

### APPENDIX C: SENSITIVITY OF THE COMPOSITE SPREAD MODEL

The components of composite spread model introduced in Sec. II B, include the laminar and turbulent vorticity thicknesses,  $\delta_l(x)$  and  $\delta_t(x)$ , respectively, and the spline parameters  $x_m$  and  $l_m$ .

For the cases of Table I, this spline curve reduces to

$$\begin{aligned} \delta_w(x) = & \delta_w\left(x_m - \frac{l_m}{2}\right)\left(\frac{x_m - x}{l_m} + \frac{1}{2}\right) + \delta_w\left(x_m + \frac{l_m}{2}\right)\left(\frac{x - x_m}{l_m} + \frac{1}{2}\right) \\ & + A\left[x^2 - 2x_m x + \left(x_m + \frac{l_m}{2}\right)\left(x_m - \frac{l_m}{2}\right)\right], \end{aligned} \quad (\text{C1})$$

where  $x_m$  lies at the middle of the length  $l_m$  and the constant  $A$  varies, which for the case K00 is  $A \approx 1.13 \times 10^{-4}$ . The laminar and turbulent vorticity thicknesses as given via (18) and (20), respectively, are standard results, whereas the choice of spline curve in Eq. (C1) that blends between these two regimes may seem *ad hoc*, which we now show via a sensitivity analysis to be unimportant in a linear setting.

Figure 12 shows the evolution of composite spread curves and the corresponding modal energies, as  $x_m$  is varied with the width  $l_m = 120$  held constant, for the case K00 of Table I. In Fig. 12(b) the approximate saturation locations of the respective energy curves are labeled via vertical lines,

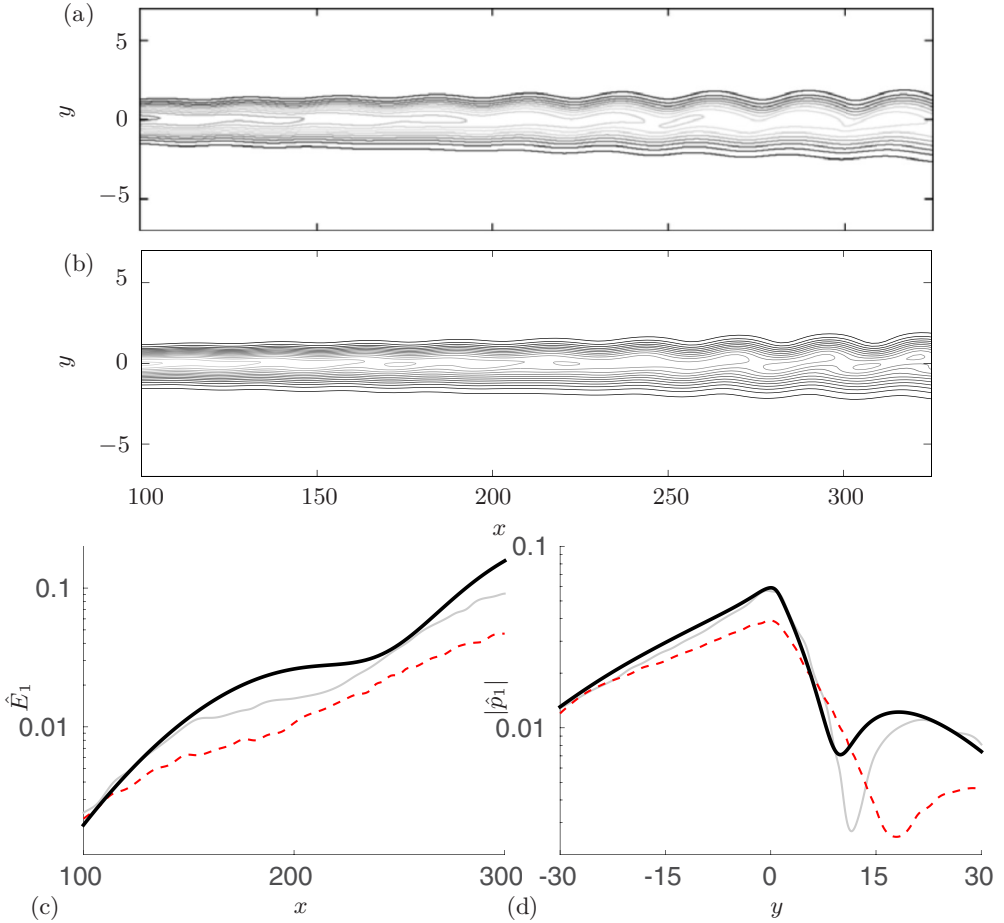


FIG. 10. Comparison of linear PSE results of the most unstable mode for a supersonic mixing layer M29M1 [23] with its DNS [23] for the following: spanwise vorticity contours between (a) DNS and (b) linear PSE; variation of (c)  $\hat{E}_1(x)$  and (d) pressure  $|\hat{p}_1(y)|$  at  $x = 275$ . In (c) and (d) (solid black line) linear PSE, (dashed line) DNS and a (solid grey line) nonlinear PSE solution [23] are shown.

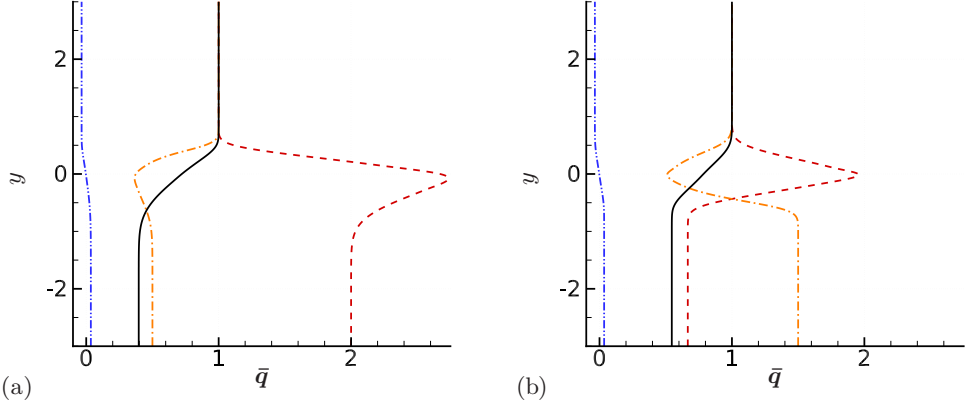


FIG. 11. Mean profiles of  $\bar{u}$ ;  $\bar{T}$ ;  $\bar{\rho}$ ; and  $\bar{Z}$  shown for cases (a) F1010 and (b) S1010 of Table I.

which when compared to the vertical lines corresponding to  $x_m$  locations in Fig. 12(a) are seen to be almost identically spaced with respect to each other, indicating them to be related via a linear relationship. Also, the magnitude of saturation energy levels in Fig. 12(b) depend directly upon the length of respective  $\delta_l(x)$ , which e.g. in the  $x_m = 150$  is the longest and breaks away last from the constant-slope, exponentially growing laminar energy curve, yielding the maximum energy of the three cases, but still proportional to  $x_m$ .

In Fig. 13 the discontinuous transition location is fixed at  $x_m = 120$ , while the width of the region is varied progressively via  $l_m$ . This procedure imparts different shapes to the spline curves, where the lowest  $l_m = 60$  also produces the fastest transition to turbulence, yielding the maximum saturation modal energy. Even here, it is easy to see the levels of this saturation energy to be inversely proportional to the length  $l_m$ , while the saturation locations remain approximately unchanged.

The sensitivity analysis reported here for the case K00 of Table I may be repeated for all the other cases to yield identical conclusions. Thus, any uncertainties over the growth of transitional vorticity

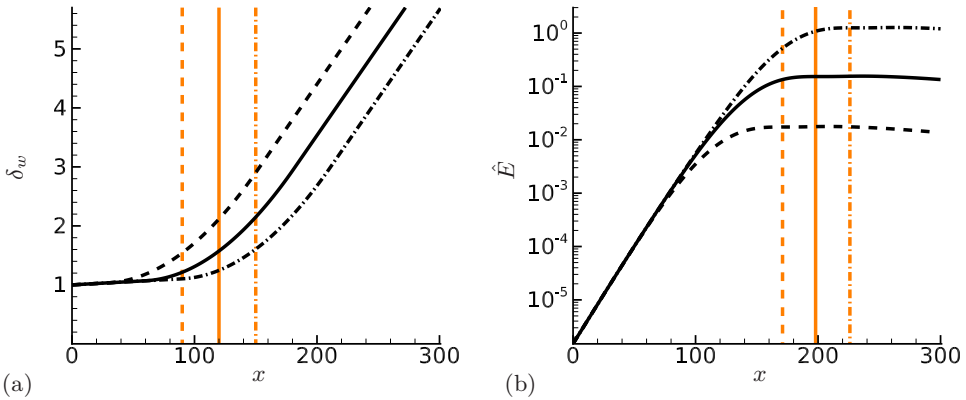


FIG. 12. Sensitivity analysis of the composite spread model with respect to the transition discontinuity ( $x_m$ ) for  $-\cdot-\cdot-$   $x_m = 90$ ;  $\text{—}$   $x_m = 120$ ; and  $\text{--}\cdot\text{--}\cdot\text{--}$   $x_m = 150$  with  $l_m = 120$  held constant, for the case K00 of Table I, showing (a) the growth of mean vorticity thicknesses and (b) the corresponding evolutions of the most unstable mode. In (a) the vertical lines indicate the respective  $x_m$  locations, while in (b) these indicate approximate locations of modal saturation.

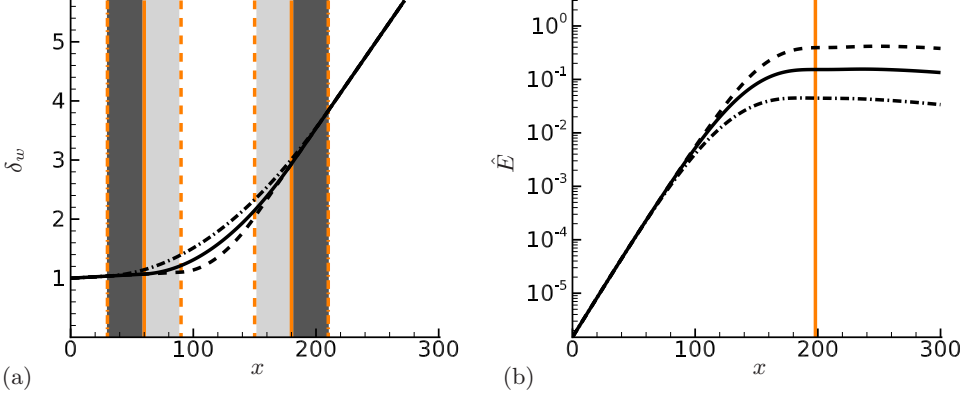


FIG. 13. Same as in Fig. 12, but for sensitivity analysis with respect to the width of transition zone ( $l_m$ ) for ---  $l_m = 60$ ; —  $l_m = 120$ ; and - · - · -  $l_m = 180$  with  $x_m = 120$  held constant. In (a) the vertical lines and the shaded areas indicate the respective widths  $l_m$ , while in (b) the vertical line is the location where all three cases approximately saturate.

thickness, modeled here via a smooth spline curve, yield only proportional changes to the modal energy evolution (and to the radiated sound), which in a linear analysis are deemed unimportant.

#### APPENDIX D: DETAILS OF PSE OPERATORS

Details of the operators appearing in Eq. (8) are given in this section:

$$\begin{aligned}
 \mathbf{A} &= \begin{pmatrix} i(\alpha_n \bar{u} - \omega_n) & i\alpha_n \bar{\rho} & 0 & 0 & 0 \\ i \frac{\alpha_n \bar{T}}{\gamma M_1^2} & i\bar{\rho}(\alpha_n \bar{u} - \omega_n) & 0 & i \frac{\alpha_n \bar{\rho}}{\gamma M_1^2} & 0 \\ 0 & 0 & i\bar{\rho}(\alpha_n \bar{u} - \omega_n) & 0 & 0 \\ 0 & i(\gamma - 1)\alpha_n \bar{\rho} \bar{T} & 0 & i\bar{\rho}(\alpha_n \bar{u} - \omega_n) & 0 \\ 0 & 0 & 0 & 0 & i\bar{\rho}(\alpha_n \bar{u} - \omega_n) \end{pmatrix}, \\
 \mathbf{B} &= \begin{pmatrix} \frac{\partial \bar{u}}{\partial x} + \frac{\partial \bar{v}}{\partial y} & \frac{\partial \bar{\rho}}{\partial x} & \frac{\partial \bar{\rho}}{\partial y} & 0 & 0 \\ \bar{u} \frac{\partial \bar{u}}{\partial x} + \bar{v} \frac{\partial \bar{u}}{\partial y} + \frac{1}{\gamma M_1^2} \frac{\partial \bar{T}}{\partial x} & \bar{\rho} \frac{\partial \bar{u}}{\partial x} & \bar{\rho} \frac{\partial \bar{u}}{\partial y} & \frac{1}{\gamma M_1^2} \frac{\partial \bar{\rho}}{\partial x} & 0 \\ \bar{u} \frac{\partial \bar{v}}{\partial x} + \bar{v} \frac{\partial \bar{v}}{\partial y} + \frac{1}{\gamma M_1^2} \frac{\partial \bar{T}}{\partial y} & \bar{\rho} \frac{\partial \bar{v}}{\partial x} & \bar{\rho} \frac{\partial \bar{v}}{\partial y} & \frac{1}{\gamma M_1^2} \frac{\partial \bar{\rho}}{\partial y} & 0 \\ (\gamma - 1)\bar{T} \left( \frac{\partial \bar{u}}{\partial x} + \frac{\partial \bar{v}}{\partial y} \right) + \bar{u} \frac{\partial \bar{T}}{\partial x} + \bar{v} \frac{\partial \bar{T}}{\partial y} & \bar{\rho} \frac{\partial \bar{T}}{\partial x} & \bar{\rho} \frac{\partial \bar{T}}{\partial y} & (\gamma - 1)\bar{\rho} \left( \frac{\partial \bar{u}}{\partial x} + \frac{\partial \bar{v}}{\partial y} \right) & 0 \\ \bar{u} \frac{\partial \bar{Z}}{\partial x} + \bar{v} \frac{\partial \bar{Z}}{\partial y} & \bar{\rho} \frac{\partial \bar{Z}}{\partial x} & \bar{\rho} \frac{\partial \bar{Z}}{\partial y} & 0 & 0 \end{pmatrix}, \\
 \mathbf{C} &= \begin{pmatrix} \bar{u} & \bar{\rho} & 0 & 0 & 0 \\ \frac{\bar{T}}{\gamma M_1^2} & \bar{\rho} \bar{u} & 0 & \frac{\bar{\rho}}{\gamma M_1^2} & 0 \\ 0 & 0 & \bar{\rho} \bar{u} & 0 & 0 \\ 0 & (\gamma - 1)\bar{\rho} \bar{T} & 0 & \bar{\rho} \bar{u} & 0 \\ 0 & 0 & 0 & 0 & \bar{\rho} \bar{u} \end{pmatrix},
 \end{aligned}$$

$$\mathbf{D} = \begin{pmatrix} \bar{v} & 0 & \bar{\rho} & 0 & 0 \\ 0 & \bar{\rho}\bar{v} & 0 & 0 & 0 \\ \frac{\bar{T}}{\gamma M_1^2} & 0 & \bar{\rho}\bar{v} & \frac{\bar{p}}{\gamma M_1^2} & 0 \\ 0 & 0 & (\gamma - 1)\bar{\rho}\bar{T} & \bar{\rho}\bar{v} & 0 \\ 0 & 0 & 0 & 0 & \bar{\rho}\bar{v} \end{pmatrix},$$

$$\mathbf{E} \equiv \mathbf{E}_2 \frac{\partial^2}{\partial y^2} + \mathbf{E}_1 \frac{\partial}{\partial y},$$

$$\mathbf{E}_1 = \gamma(\gamma - 1)M_1^2 \begin{pmatrix} 0 & 0 & 0 & 0 & 0 \\ 0 & 0 & 0 & 0 & 0 \\ 0 & 0 & 0 & 0 & 0 \\ 0 & 2\bar{\mu} \frac{\partial \bar{\mu}}{\partial y} & \frac{8\bar{\mu}}{3} \frac{\partial \bar{v}}{\partial y} & 0 & 0 \\ 0 & 0 & 0 & 0 & 0 \end{pmatrix},$$

$$\mathbf{E}_2 = \begin{pmatrix} 0 & 0 & 0 & 0 & 0 \\ 0 & \bar{\mu} & 0 & 0 & 0 \\ 0 & 0 & \frac{4}{3}\bar{\mu} & 0 & 0 \\ 0 & 0 & 0 & \frac{\gamma\bar{\mu}}{\text{Pr}} & 0 \\ 0 & 0 & 0 & 0 & \frac{\bar{\mu}}{\text{PrLe}} \end{pmatrix}.$$

- 
- [1] M. J. T. Smith, *Aircraft Noise* (Cambridge University Press, Cambridge, UK, 2004).
- [2] H. A. Hassan, Scaling of combustion-generated noise, *J. Fluid Mech.* **66**, 445 (1974).
- [3] W. C. Strahle, Combustion noise, *Prog. Energy Combust. Sci.* **4**, 157 (1978).
- [4] A. P. Dowling and S. R. Stow, Acoustic analysis of gas turbine combustors, *J. Propul. Power* **19**, 751 (2003).
- [5] T. Liewen and V. Yang, *Combustion Instabilities in Gas Turbine Engines. Operational Experience, Fundamental Mechanisms and Modeling*, Progress in Astronautics and Aeronautics, Vol. 210 (AIAA, 2005).
- [6] S. A. Klein and J. B. W. Kok, Sound generation by turbulent nonpremixed flames, *Combust. Sci. Technol.* **149**, 267 (1999).
- [7] M. Ihme, H. Pitsch, and D. Bodony, Radiation of noise in turbulent nonpremixed flames, *Proc. Combust. Inst.* **32**, 1545 (2009).
- [8] M. Ihme and H. Pitsch, On the generation of direct combustion noise in turbulent non-premixed flames, *Int. J. Aeroacoustics* **11**, 25 (2012).
- [9] A. P. Dowling and Y. Mahmoudi, Radiation of noise in turbulent non-premixed flames, *Proc. Combust. Inst.* **35**, 65 (2015).
- [10] K. K. Singh, S. H. Frankel, and J. P. Gore, Study of spectral noise emissions from standard turbulent nonpremixed flames, *AIAA J.* **42**, 931 (2004).
- [11] F. Flemming, A. Sadiki, and J. Janicka, Investigation of combustion noise using a LES/CAA hybrid approach, *Proc. Combust. Inst.* **31**, 3189 (2007).
- [12] S. L. Bragg, Combustion noise, *J. Inst. Fuel* **36**, 12 (1963).
- [13] W. C. Strahle, On combustion generated noise, *J. Fluid Mech.* **49**, 399 (1971).
- [14] W. Zhao and S. H. Frankel, Numerical simulations of sound radiated from an axisymmetric premixed reacting jet, *Phys. Fluids* **13**, 2671 (2001).
- [15] F. P. Bertolotti and T. Herbert, Analysis of the linear stability of compressible boundary layers using the PSE, *Theor. Comput. Fluid Dyn.* **3**, 117 (1991).



- [16] T. Herbert, Parabolized stability equations, *Annu. Rev. Fluid Mech.* **29**, 245 (1997).
- [17] C. K. W. Tam and P. J. Morris, The radiation of sound by the instability waves of a compressible plane turbulent shear layer, *J. Fluid Mech.* **98**, 349 (1980).
- [18] C. K. W. Tam and D. Burton, Sound generation by instability waves of supersonic flows. Part 1. Two dimensional mixing layers, *J. Fluid Mech.* **138**, 249 (1984).
- [19] E. J. Avital, N. D. Sandham, and K. H. Luo, Mach wave radiations by mixing layers. Part I: Analysis of the sound field, *Theor. Comput. Fluid Dyn.* **12**, 73 (1998).
- [20] E. J. Avital, N. D. Sandham, and K. H. Luo, Mach wave radiations by mixing layers. Part II: Analysis of the source field, *Theor. Comput. Fluid Dyn.* **12**, 91 (1998).
- [21] X. S. Wu, Mach wave radiation of nonlinear evolving supersonic instability modes in shear layers, *J. Fluid Mech.* **523**, 121 (2005).
- [22] N. D. Sandham, C. L. Morfey, and W. Z. Hu, Nonlinear mechanisms of sound generation in a perturbed parallel flow, *J. Fluid Mech.* **565**, 1 (2006).
- [23] L. C. Cheung and S. K. Lele, Linear and nonlinear processes in two-dimensional mixing layer dynamics and sound radiation, *J. Fluid Mech.* **625**, 321 (2009).
- [24] G. L. Brown and A. Roshko, On density effects and large structures in turbulent mixing layers, *J. Fluid Mech.* **64**, 775 (1974).
- [25] C. D. Winant and F. K. Browand, Vortex pairing : The mechanism of turbulent mixing-layer growth at moderate Reynolds number, *J. Fluid Mech.* **63**, 237 (1974).
- [26] N. D. Sandham and W. C. Reynolds, Three-dimensional simulations of large eddies in the compressible mixing layer, *J. Fluid Mech.* **224**, 133 (1991).
- [27] N. T. Clemens and M. G. Mungal, Large-scale structure and entrainment in the supersonic mixing layer, *J. Fluid Mech.* **284**, 171 (1995).
- [28] A. W. Vreman, N. D. Sandham, and K. H. Luo, Compressible mixing layer growth rate and turbulence characteristics, *J. Fluid Mech.* **320**, 235 (1996).
- [29] C. Pantano and S. Sarkar, A study of compressible effects in the high-speed turbulent shear layer using direct simulation, *J. Fluid Mech.* **451**, 329 (2002).
- [30] R. Rajaram and T. Lieuwen, Parametric studies of acoustic radiation from turbulent premixed flames, *Combust. Sci. Technol.* **175**, 2269 (2003).
- [31] G. Batchelor and A. E. Gill, Analysis of the stability of axisymmetric jets, *J. Fluid Mech.* **14**, 529 (1962).
- [32] S. C. Crow and F. H. Champagne, Orderly structure in jet turbulence, *J. Fluid Mech.* **48**, 547 (1971).
- [33] G. E. Mattingly and C. C. Chang, Unstable waves on an axisymmetric jet column, *J. Fluid Mech.* **65**, 541 (1971).
- [34] D. G. Crighton and M. Gaster, Stability of slowly diverging jet flows, *J. Fluid Mech.* **77**, 397 (1976).
- [35] A. Michalke, Survey on jet instability theory, *Prog. Aerosp. Sci.* **21**, 159 (1984).
- [36] C. K. W. Tam and P. J. Morris, Tone excited jets, part V: A theoretical model and comparison with experiment, *J. Sound Vib.* **102**, 119 (1985).
- [37] M. R. Malik and C. L. Chang, Nonparallel and nonlinear stability of supersonic jetflow, *Comput. Fluids* **29**, 327 (2000).
- [38] M. J. Day, N. N. Mansour, and W. C. Reynolds, Nonlinear stability and structure of compressible reacting mixing layers, *J. Fluid Mech.* **446**, 375 (2001).
- [39] P. K. Ray, L. C. Cheung, and S. K. Lele, On the growth and propagation of linear instability waves in compressible turbulent jets, *Phys. Fluids* **21**, 054106 (2009).
- [40] L. C. Cheung and S. K. Lele, The dynamics of nonlinear instability waves in laminar heated and unheated compressible mixing layers, *Phys. Fluids* **21**, 094103 (2009).
- [41] K. Gudmundsson and T. Colonius, Instability wave models for the near-field fluctuations of turbulent jets, *J. Fluid Mech.* **689**, 97 (2011).
- [42] A. Sinha, D. Rodriguez, G. Brès, and T. Colonius, Wavepacket models for supersonic jet noise, *J. Fluid Mech.* **742**, 71 (2014).
- [43] A. V. G. Cavalieri, P. Jordan, A. Agarwal, and Y. Gervais, Jittering wave-packet models for subsonic jet noise, *J. Sound Vib.* **330**, 4474 (2011).

- [44] A. Towne, T. Colonius, P. Jordan, A. V. G. Cavalieri, and G. A. Brès, Stochastic and nonlinear forcing of wavepackets in a Mach 0.9 jet, in *Proceedings of the 21st AIAA/CEAS Aeroacoustics Conference, Dallas, TX, USA* (AIAA, Reston, USA, 2015), Paper 2015–2217.
- [45] A. V. G. Cavalieri and A. Agarwal, Coherence decay and its impact on sound radiation by wavepackets, *J. Fluid Mech.* **748**, 399 (2014).
- [46] K. Mohseni, T. Colonius, and J. B. Freund, An evaluation of linear instability waves as sources of sound in a supersonic turbulent jet, *Phys. Fluids* **14**, 3593 (2002).
- [47] M. E. Goldstein and S. J. Leib, The role of instability waves in predicting jet noise, *J. Fluid Mech.* **525**, 37 (2005).
- [48] H. Gropengiesser, Study on the stability of boundary layers and compressible fluids, NASA Technical Translation TT F-12786 (NASA, 1970).
- [49] T. L. Jackson and C. E. Grosch, Inviscid spatial stability of a compressible mixing layer, *J. Fluid Mech.* **208**, 609 (1989).
- [50] T. L. Jackson and C. E. Grosch, Inviscid spatial stability of a compressible mixing layer. Part 2. The flame sheet model, *J. Fluid Mech.* **217**, 391 (1990).
- [51] O. H. Planche and W. C. Reynolds, Heat release effects on mixing in supersonic reacting free shear layers, in *Proceedings of the 30th Aerospace Sciences Meeting & Exhibit, Reno, NV, USA* (AIAA, Reston, USA, 1992), Paper 92–0092.
- [52] D. S. Shin and J. H. Ferziger, Linear stability of the compressible reacting mixing layer, *AIAA J.* **31**, 677 (1993).
- [53] C. K. W. Tam, Directional acoustic radiation from a supersonic jet generated by shear layer instability, *J. Fluid Mech.* **46**, 757 (1971).
- [54] C. K. W. Tam, Supersonic jet noise, *Annu. Rev. Fluid Mech.* **27**, 17 (1995).
- [55] D. Papamoschou and A. Roshko, The compressible turbulent shear layer: An experimental study, *J. Fluid Mech.* **197**, 453 (1988).
- [56] A. Samanta, On the axisymmetric stability of heated supersonic round jets, *Proc. R. Soc. London A* **472**, 20150817 (2016).
- [57] J. C. Hermanson and P. E. Dimotakis, Effects of heat release in a turbulent, reacting shear layer, *J. Fluid Mech.* **199**, 333 (1989).
- [58] A. Sharma and S. K. Lele, Effects of heating on noise radiation from a two-dimensional mixing layer: Direct computations and acoustic analogy predictions, in *Proceedings of the 17th AIAA/CEAS Aeroacoustics Conference, Portland, OR, USA* (AIAA, Reston, USA, 2011), Paper 2011–2744.
- [59] F. A. Williams, *Combustion Theory*, 2nd ed. (The Benjamin/Cummins Publishing Company, Menlo Park, USA, 1985).
- [60] Y. C. See and M. Ihme, Effects of finite-rate chemistry and detailed transport on the instability of jet diffusion flames, *J. Fluid Mech.* **745**, 647 (2014).
- [61] D. Rodriguez, A. Samanta, A. V. G. Cavalieri, T. Colonius, and P. Jordan, Parabolized stability equation models for predicting large-scale mixing noise of turbulent round jets, in *Proceedings of the 17th AIAA/CEAS Aeroacoustics Conference, Portland, OR, USA* (AIAA, Reston, USA, 2011), Paper 2011–2838.
- [62] D. S. Shin and J. H. Ferziger, Linear stability of the reacting mixing layer, *AIAA J.* **29**, 1634 (1991).
- [63] Kenneth K. Kuo, *Principles of Combustion*, 2nd ed. (John Wiley & Sons, Hoboken, USA, 2005).
- [64] H. Schlichting and K. Gersten, *Boundary-Layer Theory*, 8th ed. (Springer-Verlag Berlin, 2000).
- [65] M. J. Day, Structure and stability of compressible reacting mixing layers, Ph.D. thesis, Stanford University, 1999.
- [66] M. F. Barone, W. L. Oberkampf, and F. G. Blottner, Validation case study: Prediction of compressible turbulent mixing layer growth rate, *AIAA J.* **44**, 1488 (2006).
- [67] M. E. Goldstein, An exact form of Lilley’s equation with a velocity quadrupole/temperature dipole source term, *J. Fluid Mech.* **443**, 231 (2001).
- [68] T. Herbert, Parabolized stability equations, Tech. Rep., AGARD-FDP-VK 1. Special Course on Progress in Transition Modeling, AGARD-R-793 (1994).

- [69] P. Shivakanthchary, Linear models for reacting mixing layers, Master's thesis, Indian Institute of Science, 2016.
- [70] F. Li and M. R. Malik, Spectral analysis of parabolized stability equations, *Comput. Fluids* **26**, 279 (1997).
- [71] M. Lessen, J. A. Fox, and H. M. Zien, Stability of the laminar mixing of two parallel streams with respect to supersonic disturbances, *J. Fluid Mech.* **25**, 737 (1966).
- [72] B. T. Chu, On the energy transfer to small disturbances in fluid flow (Part I), *Acta Mech.* **1**, 215 (1965).
- [73] C. K. W. Tam and F. Q. Hu, On the three families of instability waves of high-speed jets, *J. Fluid Mech.* **201**, 447 (1989).
- [74] O. Zeman, Dilatation dissipation: The concept and application in modeling compressible mixing layers, *Phys. Fluids A* **2**, 178 (1990).
- [75] C. K. W. Tam, Mach wave radiation from high-speed jets, *AIAA J.* **47**, 2440 (2009).
- [76] S. Kotake and K. Takamoto, Combustion noise: Effects of the shape and size of burner nozzle, *J. Sound Vib.* **112**, 345 (1987).
- [77] K. K. Singh, C. Zhang, J. P. Gore, L. Mongeau, and S. H. Frankel, An experimental study of partially premixed flame sound, *Proc. Combust. Inst.* **30**, 1707 (2005).
- [78] R. Rajaram and T. Lieuwen, Acoustic radiation from turbulent premixed flames, *J. Fluid Mech.* **637**, 357 (2009).
- [79] L. Kabiraj, H. Nawroth, A. Saurabh, and C. O. Paschereit, Experimental study of noise generation by a turbulent premixed flame, in *Proceedings of the 19th AIAA/CEAS Aeroacoustics Conference, Berlin, Germany* (AIAA, Reston, USA, 2013), Paper 2013–2002.
- [80] N. D. Sandham and W. C. Reynolds, A Numerical Investigation of the Compressible Mixing Layer, Tech. Rep. TF-45, Mechanical Engineering Department, Stanford University (1989).